Algal Research 93 (2026) 104479

Contents lists available at ScienceDirect

Algal Research

journal homepage: www.elsevier.com/locate/algal

Multi-omics dissect the molecular mechanisms driving high-lipid production in a laboratory-evolved *Chlamydomonas* mutant

David R. Nelson [a,1,*], Amphun Chaiboonchoe [a,g,1,*], Weiqi Fu [a,b,1,*], Basel Khraiwesh [a,c], Bushra Dohai [a,h], Ashish Jaiswal [a], Dina Al-Khairy [a], Alexandra Mystikou [a,i], Latifa Al Nahyan [d], Amnah Salem Alzahmi [a,k], Layanne Nayfeh [a], Sarah Daakour [a], Matthew J. O'Connor [e], Mehar Sultana [c,e], Khaled M. Hazzouri [c,j], Jean-Claude Twizere [a,f,k], Kourosh Salehi-Ashtiani [a,*]

[a] *Division of Science, New York University Abu Dhabi, P.O. Box 129188, Abu Dhabi, United Arab Emirates*
[b] *State Key Laboratory of Ocean Sensing & Ocean College, Zhejiang University, Zhoushan, 316021, China*
[c] *Center for Genomics and Systems Biology (CGSB), New York University Abu Dhabi, P.O. Box 129188, Abu Dhabi, United Arab Emirates*
[d] *Al Yasmina Academy, Abu Dhabi, United Arab Emirates*
[e] *Core Technology Platform (CTP) Operations, New York University Abu Dhabi, P.O. Box 129188, Abu Dhabi, United Arab Emirates*
[f] *Laboratory of Viral Interactomes, GIGA Institute, University of Liege, Belgium*
[g] *Siriraj Center of Research Excellence for Precision Medicine and Systems Pharmacology (SiCORE-PM&SP), Department of Pharmacology, Faculty of Medicine, Siriraj Hospital, Mahidol University, Bangkok, 10700, Thailand*
[h] *Institute of Network Biology (INET), Molecular Targets and Therapeutics Center (MTTC), Helmholtz Munich, German Research Center for Environmental Health, Neuherberg, Germany*
[i] *Omics Centre of Excellence, M42 Health, Abu Dhabi, United Arab Emirates*
[j] *Khalifa Center for Genetic Engineering and Biotechnology (KCGEB), UAE University, Al Ain, Abu Dhabi, United Arab Emirates*
[k] *Terra Research Centre, Gembloux Agro Bio-Tech, University of Liege, Gembloux, Belgium*

ARTICLE INFO

Keywords:
Chlamydomonas
Microalgae
Mutagenesis
Lipids
Genomics
Transcriptomics
Metabolomics

ABSTRACT

Enhancing lipid accumulation in microalgae is critical for commercial viability but often compromises growth. We previously generated through UV mutagenesis and iterative selection a *Chlamydomonas reinhardtii* mutant (H5) that retains parental growth while producing 3.2-fold more lipids (Sharma et al., 2015; Abdrabu et al., n.d.). Here, we present multi-omic analyses elucidating the molecular basis of this phenotype. Whole-genome sequencing revealed over 3000 mutations including a frameshift in the regulatory domain of 6-phosphofructokinase (PFK1). Six independent CLiP mutants in affected genes also showed elevated lipids, including a PFK1 mutant, validating functional relevance. Transcriptomics revealed upregulation of glycolytic genes and nutrient acquisition pathways under nutrient-replete conditions. Metabolomics identified an 8.31-fold malonate increase ($p = 8.5 \times 10^{-4}$), linking glycolysis to lipid synthesis. Lipidomics showed increased TAG diversity and lack of betaine lipids. Epigenomics revealed genome-wide hypermethylation, potentially stabilizing the phenotype. Together, these data suggest PFK1 deregulation drives metabolic reprogramming enabling lipid accumulation without growth penalty, demonstrating how evolutionary selection generates sophisticated metabolic solutions for engineering industrial microalgal strains.

1. Introduction

Algae are a promising platform for sustainable production of biofuels, pharmaceuticals, and other high-value products, due to their rapid growth and capacity to thrive on non-arable land [3–6]. Unlike land crops, they support continuous, season-independent cultivation [7,8] and can be grown in regions unsuitable for agriculture, offering an alternative to deforestation-linked crops like oil palm [9–12].

Overcoming the growth-lipid tradeoff represents the primary technological barrier to economically viable algal biofuel production.

* Corresponding authors.
E-mail addresses: drn2@nyu.edu (D.R. Nelson), amphun.cha@mahidol.ac.th (A. Chaiboonchoe), weiqifu@zju.edu.cn (W. Fu), ksa3@nyu.edu (K. Salehi-Ashtiani).
[1] These authors contributed equally to this work.

https://doi.org/10.1016/j.algal.2025.104479
Received 5 August 2025; Received in revised form 16 October 2025; Accepted 8 December 2025
Available online 15 December 2025

Current yields fall short of the theoretical maximum by orders of magnitude, making algal oils more expensive than petroleum alternatives. While genetic engineering approaches have achieved incremental improvements, they often suffer from genetic instability, regulatory challenges, and unexpected metabolic bottlenecks. This study addresses these limitations through a comprehensive multi-omics dissection of a stable, high-lipid mutant (H5) that maintains normal growth, providing fundamental insights into metabolic regulation and practical targets for strain engineering.

Our approach considers "cancer-like" metabolic reprogramming as a biotechnological strategy. We describe H5's metabolism as "cancer-like" based on specific metabolic parallels and not as a literal comparison to cancer cells. This terminology, established in the metabolic engineering literature, refers to the reprogramming strategy of enhanced glycolysis (Warburg effect), increased anabolic metabolism, altered mitochondrial function, epigenomic hypermethylation, and constitutive growth signaling. While pathological in multicellular organisms, these features can be advantageous for industrial microorganisms where maximizing product yield is paramount. By understanding how such metabolic shifts arise and stabilize in the H5 mutant, we can use this paradigm—redirecting cellular resources from maintenance to production—as a blueprint for engineering high-productivity industrial strains.

In commercial microalgal lipid production scenarios, lipid accumulation competes with cell proliferation for energy and carbon, creating a trade-off that limits productivity [13]. Fatty acids can be routed either to membrane synthesis or to intracellular lipid bodies—the latter being most relevant for industrial applications [13]. Wild-type strains typically exhibit low lipid content, and while transgenic efforts have achieved incremental improvements, they often face instability or reduced growth. Overcoming the growth–lipid tradeoff is essential for profitable algal oil production, yet current engineering approaches are insufficient for sustained gains [14].

Chlamydomonas reinhardtii has arguably been the most popular and well-studied green microalga to date. *Chlamydomonas*, although not oleaginous by definition, is widely used to study microalgal lipid metabolism because it, like many other microalgae, accumulates triacylglycerols under various conditions [15]. Our study focuses on a high-lipid *C. reinhardtii* mutant (named 'H5') with multiple mutations. We aim to understand the underlying mechanisms in artificial laboratory evolution (ALE) to produce a synthetic microbial chassis suitable for profitable biotechnological lipid production in microalgae. Specifically, we target microalgae growing exponentially, working towards a continuous production system for microalgal lipids.

Our previous work demonstrated that UV mutagenesis combined with iterative FACS-based selection can increase lipid accumulation in microalgae [1,2]. Using this approach, we generated the *C. reinhardtii* mutant H5 (CC-5163, available at https://www.Chlamycollection.org) from parental strain CC-503 [2]. Initial characterization previously showed that H5 accumulates 3.2-fold more lipids than CC-503 during

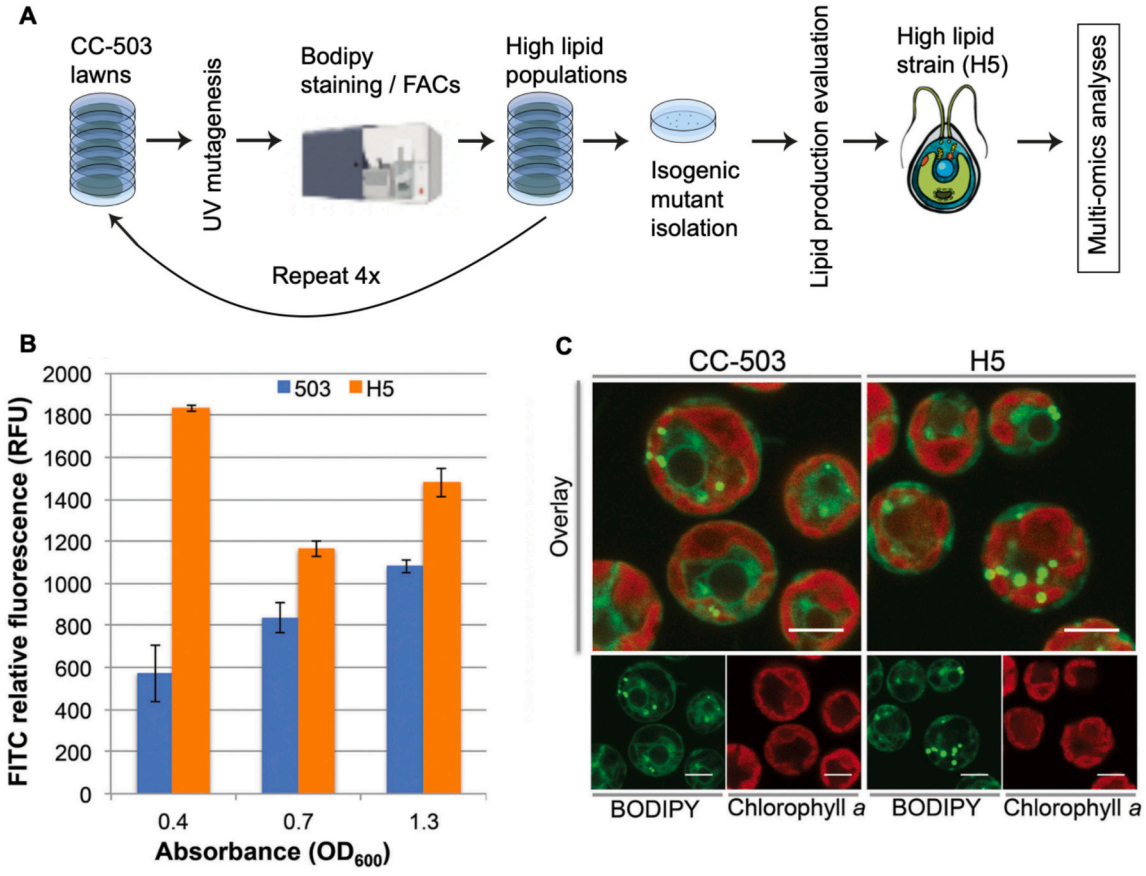

Fig. 1. Introductory figure. Mutant generation rationale and phenotype from previous work [2].
(A) Schematic diagram showing the overall experimental procedure to generate high-lipid *C. reinhardtii* strains (adapted from Abdrabu et al. [2] and Sharma et al. [1]). One of four high-lipid mutants (H5) generated was chosen for in-depth-omics analyses for the current study because it accumulated lipids during exponential phase.
(B) Flow cytometry-based fluorescence intensity measurements for BODIPY 505/515-stained *C. reinhardtii* cells in different growth phases indicated by their optical density. Standard error is shown. H5 cells accumulated significantly more lipids in the exponential growth phase (OD_{600} = 0.4), as observed in previous work [2].
(C) Confocal fluorescence microscopy of BODIPY 505/515-stained CC-503 and H5 strains contrasted by chlorophyll autofluorescence during the exponential growth phase. Scale bar indicates 5 μm.

exponential growth (OD600 = 0.4) while maintaining parental growth rates, as measured by BODIPY™ 505/515 (4,4-Difluoro-1,3,5,7-Tetramethyl-4-Bora-3a,4a-Diaza-s-Indacene; Invitrogen, Carlsbad, California, USA) staining and flow cytometry (Fig. 1). The fluorescent dye–based assay has been repeatedly validated as a reliable approach for the relative quantification of neutral lipid content [16–20].

However, the molecular mechanisms underlying this unusual phenotype—overcoming the typical growth-lipid tradeoff—remained unknown. Here, we used an integrative multi-omics approach to dissect the genetic, transcriptional, metabolic, and epigenetic basis of H5's enhanced lipid production. Whole-genome resequencing identified UV-induced mutations in key metabolic genes, including a frameshift in the regulatory domain of 6-phosphofructokinase (PFK1). Transcriptomic analysis revealed constitutive upregulation of glycolytic and stress-responsive genes under nutrient-replete conditions. Metabolomic profiling uncovered an 8.31-fold increase in malonate, linking deregulated glycolysis to fatty acid synthesis, while comprehensive LC-MS/QToF lipidomics (Fig. 4, Data S1) provided molecular-level characterization of specific TAG, DAG, and fatty acid species. Epigenomic analysis demonstrated genome-wide hypermethylation potentially stabilizing the multi-mutation phenotype. Together, these data reveal how multiple mutations synergistically reprogram cellular metabolism to achieve stable, high-productivity lipid accumulation, providing a blueprint for engineering commercially viable microalgal strains.

2. Materials and methods

2.1. Algal strains, culture conditions, and growth analysis

C. reinhardtii strain CC-503 was purchased from the *Chlamydomonas* Resource Center (http://Chlamycollection.org), and H5 was generated from our previous study [1]. We deposited H5 in the *Chlamydomonas* Resource Center (CC-5163 H5-M1 mt+ (high lipid-producing strain)) (https://www.Chlamycollection.org/product/cc-5163-h5-m1-mt-high-lipid-producing/). *C. reinhardtii* cultures were grown on tris-acetate-phosphate medium [21] using constant lights with an intensity of 400 μmol photons m^{-2} s^{-1}. The pond simulators PBR101 (Phenometrics, Inc., Michigan, USA) were approximately cylinder photobioreactors (PBRs). They were set up with a working volume of 360 mL and a light depth of 14.0 cm for each working PBR. The PBRs were injected with air enriched with 1.0 % CO_2 at a flow rate of 0.36 L/min. Temperature and pH were maintained at 25 ± 1 °C and 7.0 ± 0.5, respectively. Stirring was set at a constant speed of 100 RPM using a 28.6 mm stir bar. Cell diameter and size distribution were determined using the Cellometer Auto M10 (Nexcelom Bioscience LLC, Lawrence, MA, USA). The growth and FACS were carried out on H5 and CC-503 strains obtained from the *Chlamydomonas* Resource Center (https://www.Chlamycollection.org, St. Paul, MN, USA).

2.2. Generation of genome sequence and assembly of H5 and variant detection

CC-503 and the H5 mutant single colony that produced the highest FACS signal were selected for genome sequencing. Genomic PCR-free sequencing of H5 by HISeq2500 and single nucleotide polymorphism (SNP) calling was run to determine nucleotide differences between CC-503 and H5. We used Bowtie2 [22] to align the reads with the reference genome PhytozomeV10/Creinhardtii/Creinhardtii_281_v5.0.fa. Candidate SNPs were identified using SAMtools [23]. SnpEff [24] was used to annotate detected variants with default parameters using *C. reinhardtii*_281_v5.0 as a database. We focused on 'high-impact' mutations for phenotype attributions. The scale of impact in SnpEff was measured as the 'effect' variable (EFF) where EFF = Effect (Effect_Impact | Functional_Class | Codon_Change | Amino_Acid_Change| Amino_Acid_Length | Gene_Name | Transcript_BioType | Gene_Coding | Transcript_ID | Exon_Rank | Genotype_Number) and the multiple effects comprise the weight multiplier formula for SnpEff variant calling.

2.3. Analysis of lipid accumulation in different mutant strains using a fluorescent spectrophotometer

A group of 35 strains was purchased from *Chlamydomonas* Resource Center (http://Chlamycollection.org). These strains were sub-cultured several times to reach exponential growth in 15 mL Falcon™ tubes. The freshly prepared cultures from the exponential growth phase were used as seed cultures and transferred to 96-well microplates with a volume of 200 μL for each well and a starting OD_{600} of 0.1. After these cultures reached the exponential growth phase (OD_{600} ~ 0.4) in 96-well microplates, cells were stained with 8.0 μg/ml BODIPY 505/515 for 15 min. The cell pellets were then collected by centrifugation, washed, and resuspended with the same volume of TAP medium [21]. The fluorescence of stained cells was determined with an excitation wavelength of 485 nm and an emission wavelength of 515 nm using the hybrid multimode microplate reader Synergy H1 (BioTek Instruments, Winooski, Vermont, United States), according to the manufacturer.

2.4. Transcriptomic analysis of parental CC-503 and H5 mutant

The genome sequence of *C. reinhardtii* was used as a reference to align the transcriptome reads. Using Tuxedo suite, which includes Bowtie2 [22,25], TopHat (https://github.com/DaehwanKimLab/tophat), and Cufflinks (http://cole-trapnell-lab.github.io/cufflinks/), the raw reads were aligned to the *C. reinhardtii* reference genome (downloaded from http://genome.jgi.doe.gov/). For differentially expressed genes, we calculated FPKM values (Fragments Per Kilobase of transcript per Million mapped reads, see Table S3) [26], a normalized measure of reading density that allows transcript levels to be compared within and between samples quantitatively.

Transcriptomic sequencing (RNAseq) for CC-503 and H5 cultures in triplicates was performed at 0, 1, and 3 days of nitrogen starvation (performed as in Wang et al., [27]; see Table S3). Mid-log phase (OD_{600} = 0.4) cells were harvested for the Day 0 timepoint. To define the contributions of deprived and nutrient-replete states towards lipid accumulation in H5 and CC-503, transcriptome analyses were performed at zero, one, and three days post-inoculation in Cuffdiff [28] (Table S3). The differentially expressed genes (DEGs) were screened at false discovery rate (FDR) - corrected p values (i.e., q values) ≤ 0.05 (Table S3). At Day 0, 11,126 and 10,554 genes were expressed in CC-503 and H5 at FPKM >1.0. Of these expressed genes, 10,094 were shared between the two strains, 1032 were unique in CC-503, and 460 were unique in H5. Differentially expressed genes from Day 0 (starting point, non-starvation control) and Day 1 (deprived for 24H) comprised 1798 and 1727 upregulated transcripts and 1296 and 1602 down-^{regulated} transcripts.

The algorithm Cuffdiff [28] was used to identify differentially expressed genes (DEGs) between two groups of samples (triplicates for each group, see Table S3). Functional and gene set enrichment analysis of DEGs was performed using BiNGO [29] plugin version 3.0.3 in Cytoscape. BiNGO determined the statistical overrepresentation of the DEGs genes over the Gene Ontology (GO) terms. The p values were calculated using the hypergeometric test, and Benjamini and Hochberg False Discovery Rate (FDR) correction [30] was used to identify the statistical significance of gene ontology terms with corrected $p(q) < 0.05$ for multiple testing [29].

Transcript-level functional annotations were assigned using a custom pipeline developed in our prior work on algal metabolic network model refinement. Briefly, predicted proteins were functionally annotated using BLAST2GO as in [31], integrating BLASTP homology searches, InterProScan domain identification, and Gene Ontology (GO) term assignment. This approach provided a broad functional context based on sequence similarity to well-characterized protein families and domains.

For pathway enrichment analysis, we used the Algal Functional

Annotation Tool (AFAT, http://pathways.mcdb.ucla.edu/algal/) [32], which is specifically designed for analyzing photosynthetic eukaryotic genomes. Importantly, AFAT relies exclusively on Phytozome v5 gene accessions as its reference background, including *C. reinhardtii* and other green algae. Thus, all enrichment analyses were constrained to plant- and algae-specific orthologs, ensuring taxonomic consistency.

GO term and KEGG pathway enrichments were computed using Fisher's Exact Test with Benjamini-Hochberg correction (FDR < 0.05). KEGG pathway identifiers are based on standard KEGG nomenclature, which can result in pathway names that reference non-photosynthetic organisms (e.g., *Vibrio cholerae* infection). These labels reflect the historical origins of pathway discovery, not the taxonomic origin of genes in our dataset. For example, conserved eukaryotic processes such as vesicle trafficking and protein transport may appear under SNARE or antigen-processing pathways due to shared components, even though the genes are *Chlamydomonas*-derived.

This annotation strategy mirrors established practice in algal transcriptomic studies [31] where mixed-lineage pathway labels appear because of cross-kingdom conservation of molecular functions. To prevent confusion, we explicitly note that all gene IDs used in enrichment analyses were *C. reinhardtii* –specific, and no foreign or bacterial genes were present in our assemblies or expression sets.

2.5. Bisulfite sequencing and methylation analyses

DNA was extracted from three H5 and two CC-503 colonies (as control) using the DNeasy Plant Mini Kit (Qiagen, Hilden, Germany). Libraries were prepared using the Zymo EZ DNA Methylation Gold Kit (Zymo Research, CA, USA) and Swift Accel-NGS MethylSeq (Swift Biosciences, Inc., MI, USA). Whole Genome Bisulfite Sequencing and library preparation were carried out at Admera Health (South Plainfield, NJ, USA). For each sample, approximately 31 million 2 × 150 paired end reads were obtained. Methylation analysis was done using the bisulfate analysis package of CLC Genomics Workbench V.22 (QIAGEN, Aarhus, Denmark). Fisher's Exact Test was used to examine the statistical significance of differential methylation in CHG context (H = A, C, or T) of 100-base frames between the control and H5 reads using annotated *C. reinhardtii* transcripts (https://phytozome-next.jgi.doe.gov/info/Creinhardtii_v5_6).

2.6. HPLC-MS/QToF metabolomics analysis

For the extraction, cultured microalgae were scraped from agar plates after one week growth under approximately 100 $\mu mol \cdot m^{-2} \cdot s^{-1}$ and equal weights of three replicates for each strain were placed into 5 mL methanol then vortexed. Algal-methanol solutions were microwaved on high power (1150 W, 2450 mHz) in a ME732K microwave (Samsung, Suwon-si, South Korea) with a triple distribution system. Solutions were microwaved until boiling five times and then vortexed. Extracts were filtered with a 5 μm then 2-μm filter (Millipore, Billerica, MA, USA) and maintained in the dark at 4 °C.

The HPLC method was developed in-house and is based on a comprehensive shotgun lipidome technique [33]. Extracted metabolites were loaded on a reverse-phase C18 column starting with an elution buffer composition of 36 % 30 mM ammonium formate (AF, HCO2NH4, Chemical Abstract Services number (CAS): 540–69-2, MW: 63.06. EC Number: 208–753-9; Sigma-Aldrich, Darmstadt, DE), 36 % acetonitrile (CAN, CH3CN, Purity 99.8 %, Molecular Weight = 41.05, CAS: 50–165-7178; Sigma-Aldrich, Darmstadt, DE), and 28 % isopropanol (IPA, (CH3)2CHOH, MW: 60.10, purity ≥99.5 %, CAS: 67–63-0; Sigma-Aldrich, Darmstadt, DE). A semi-linear gradient was applied to the column resulting in 90 % isopropanol and 10 % acetonitrile for 18 min at 300 μL/min and with a column temperature of 50 °C on an Agilent 1290 Infinity II LCMS with a UHPLC column and the stream was diverted to a quadrupole time-of-flight mass spectrometer (Agilent LCMS QToF 6538, Agilent, Santa Clara, USA). Accurate mass profiling was enabled by lock mass compounds at 121.050873 and 922.009798 *m/z*. Collision energies were assigned based on the formula [1.4 * (*m/z*)/100) + 20] developed to maintain small molecule integrity and fragment larger ions.

Source datasets are in Data S1 and are comprised of high-performance liquid chromatography (HPLC) and quadrupole time-of-flight mass spectrometry (MS-QTOF, positive polarity mode) XCMS [34–37] analyses. Compound identification and comparisons were performed using nonlinear peak alignment and matching against existing databases (XCMS [34–37], HMDB [38]). This dataset includes ion abundances, total ion chromatograms (TICs)), −fold and log 2-fold change values, compound retention times, T-values, *p* values, and *q* values (*p* values adjusted for false discovery rates). Also included in the .zip file are extracted ion chromatograms (EICs) for individual compounds and boxplots of each compound compared between CC-503 and H5.

2.7. Computational metabolomics pathway analyses

Compounds identified with HPLC-MS/QToF were processed in the XCMS online software suite (https://xcmsonline.scripps.edu/. The XCMS suite integrates Lipid Maps (http://www.lipidmaps.org/), Kyoto Encylopedia for Genes and Genomes (KEGG; http://www.kegg.jp/kegg/kegg2.html), Human Metabolome Database (HMDB; http://www.hmdb.ca/), Scripps Center for Metabolomics (https://metlin.scripps.edu/index.php), the National Institute for Standards and Technology (NIST; http://webbook.nist.gov/chemistry/), and Massbank (http://www.massbank.jp) to provide a comprehensive service for identifying molecules from mass spectrometry data and comparing them between samples. The XCMS suite uses multiple pathway-based analysis tools to identify metabolic pathways from collections of candidate models, compare them between samples, and derive statistically significant results for altered levels of metabolites and pathway activity between sample groups.

Mummichog (https://shuzhao-li.github.io/mummichog.org/) was able to resolve differences in metabolic pathways for lipid metabolism. The Mummichog (1.1.6) command was: [mummichog/main.py -f H5.vs.CC.503.tsv -r ref-list.txt -k ./temp -o mummichog -m positive -n A1000047 -u 5 -c 0 -g 0]. The *C. reinhardtii* metabolic network was loaded for feature searches (BioCyc6.0). Overall, 1617 input compounds were used as queries to find 567 Mummichog compounds (518 at $p < 0.005$) from 11,892 references. Resampling was done with 100 permutations to estimate the background, and the pathway background was estimated on 33,200 random pathway values. The null distribution was estimated on 807 random modules, and our data matched seven network modules (see also Data S1).

2.8. Graphics

The figures were made using Adobe Illustrator, Adobe Photoshop, Microsoft Excel, Olympus CellSens software, Circos (circos.ca), R (3.x), Python and Matplotlib.

2.9. Statistical analyses

Biological triplicates (i.e., H5 cell populations grown from three independent colonies) were analyzed for RNAseq mapping counts to determine up- and down-regulated genes in H5 (Table S3). A Student's *t*-test was performed to evaluate the significance of the difference between the two groups of samples for growth data ($p < 0.05$). Our LC/MS-qTOF results were significant at $p < 0.05$ after correction for multiple hypotheses. Statistical metrics are included in the LC/MS-qTOF supplementary dataset describing retention time corrections and false-discovery rate-corrected *p* values [34] for matches against databases other than CHLAMY BioCyc.

3. Results and discussion

To dissect the molecular basis of H5's enhanced lipid phenotype, we took a multi-omics approach that progressively linked genetic changes to metabolic outcomes. We began with whole-genome sequencing to identify UV-induced mutations in key metabolic genes, then validated their functional impact through CLiP mutant screening. Next, we used transcriptomics to reveal how these mutations altered gene expression patterns, particularly under nutrient-replete versus nitrogen-deprived conditions, uncovering a constitutive stress-like metabolic state. Metabolomic profiling then connected these transcriptional changes to specific biochemical alterations, notably accumulation and lipidome remodeling. Finally, epigenomic analysis revealed genome-wide hypermethylation that may stabilize this reprogrammed metabolic

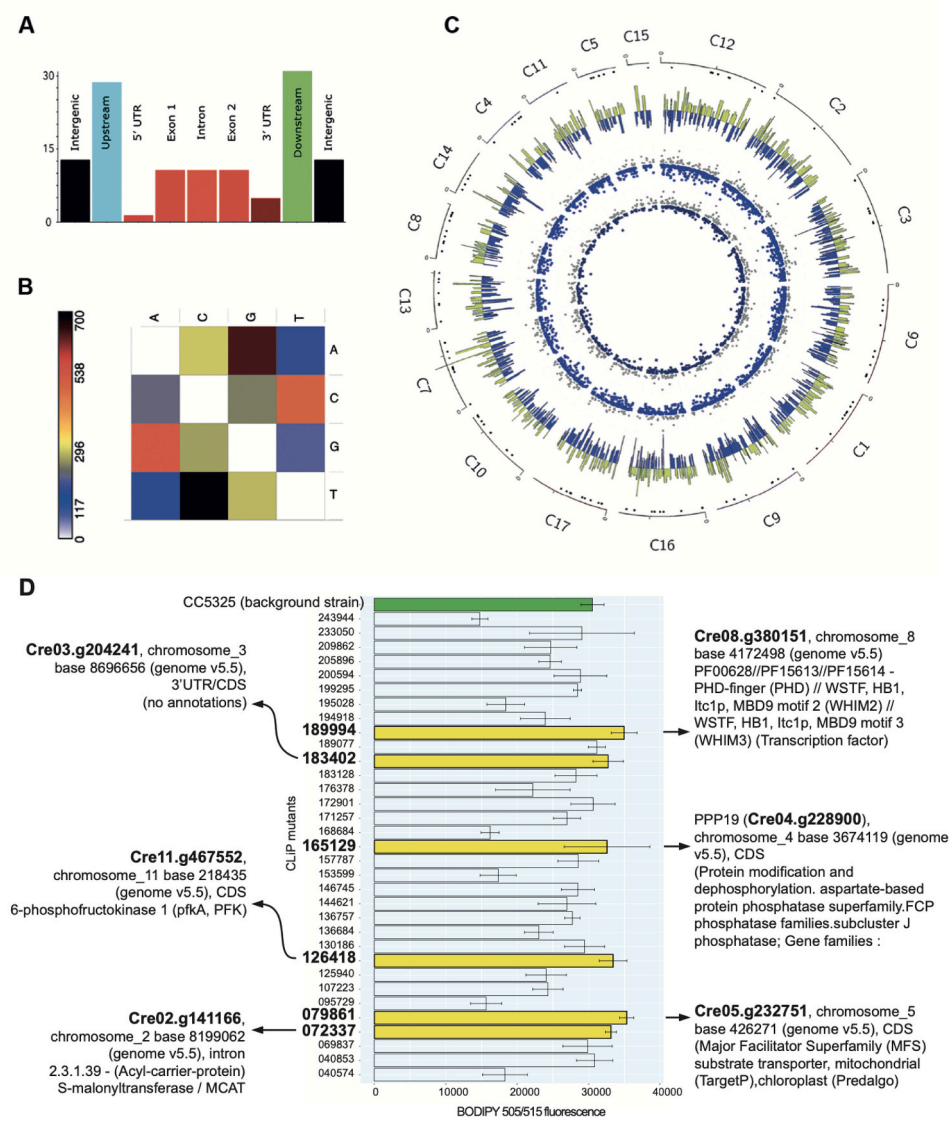

Fig. 2. Single nucleotide polymorphisms (SNPs) in the mutant H5 compared to the parental CC-503.
(A) Nucleotide variants in H5 compared to CC-503 as discovered by SnpEff [24] from genomic sequencing data ($n = 2$ for each strain, see Table S1). These variants were predicted to impact the function of their respective genes significantly. Several genes involved in metabolic pathways had frameshift mutations.
(B) A summary of total base changes for UV-induced mutations in H5. The majority of mutations observed were C → T transitions, typical products of UV-induced pyrimidine dimer repair [107].
(C) Circos (circos.ca) plot showing genomic (SNPeff-predicted mutations) and transcriptomic (RNAseq) data from H5 compared to CC-503 (see also Tables S1 and S3). The outer track shows high-impact genomic mutations, and the inner tracks indicate significant ($q < 0.05$) up and down-regulated genes in the strains for the days sampled after nitrogen deprivation. Numbered from outside to inside: 1, dots under chromosome axes represent genes with 'high-impact' mutations; 2, yellow histogram facing outwards shows genes upregulated in H5 on Day 0; 3, blue histogram facing inwards shows genes down-regulated in H5 on Day 0; 4, grey scatter plot facing outwards shows genes upregulated in H5 after 24 h of nitrogen deprivation (performed as in Wang et al., [27]; Day 1); 5, blue scatter plot facing inwards shows genes down-regulated in H5 on Day 1; 6, magenta scatter plot facing outwards shows genes upregulated in H5 after three days of nitrogen deprivation (Day 3); 7, cobalt scatterplot facing inwards shows genes down-regulated in H5 on day 3. In addition to the chromosomes shown in the above plot, several genes were up- and down-regulated in the non-chromosomal genomic scaffolds (see Fig. S2).
(D) Comparison of lipid accumulation in CLiP [50,51] strains. BODIPY 505/515 fluorescence of stained cells was determined with an excitation wavelength of 485 nm and an emission wavelength of 515. BODIPY fluorescence was normalized by OD_{600} (x-axis). Standard error is shown. The details of these CLiP mutants are in Table S1 and at Chlamylibrary.org. Six mutants had significantly higher lipid accumulation than CC-503, implying potential roles for their disrupted genes in producing the H5 high-lipid phenotype.
Induced (LCIC) protein in H5 (see Table S3). (For interpretation of the references to color in this figure legend, the reader is referred to the web version of this article.)

state. Together, these layers traced a clear mechanistic pathway from genetic disruption through transcriptional reprogramming to the observed lipid accumulation phenotype.

3.1. Whole-genome sequencing identifies variants in lipid biosynthesis pathways

A wide variety of mutagenic events, including SNPs, deletions, and inversions, can occur in eukaryotic cells in response to UV irradiation, followed by photo repair inactivation [39] during cell division [40–43]. We interrogated the underlying genetic and metabolic events that have resulted in lipid accumulation without compromising growth in H5. Whole-genome resequencing of the mutant strain revealed multiple UV-induced mutations [40–43], including SNPs, insertions, deletions, and multiple nucleotide polymorphisms (MNPs) after aligning the obtained genomic reads to the reference genome of the parent strain CC-503. Transcriptomic and metabolomic analyses revealed altered metabolism in H5, including glycerolipid and phospholipid pathways, increased expression of glycolytic enzymes and products, and a pseudo-nutrient deprivation response characterized by the upregulation of carbon, nitrogen, molybdenum, iron, and oxygen deprivation responsive genes.

We sequenced the genome of two isogenic H5 populations to characterize UV-induced mutations and their frequency and position relative to protein-coding regions. Cells grown from two independent colonies were sequenced to increase confidence in mutational event identification. After the mapping of filtered Illumina HiSeq 2500 reads to the reference CC-503 genome [44], SnpEff [24] was used to find the impacts of the variant on known genes based on the detected variants, including SNPs, insertions, deletions, and multiple nucleotide polymorphisms (MNPs). Impacts on encoded protein functions were graded as high, moderate, or low. We found 5341 variants, including 3984 SNPs, 647 insertions, and 710 deletions (Fig. 2 and Table S3). Overall SNP density and quantity was much higher on chromosomes 5, 11, 14, and 15.

Most identified variations were associated with regions upstream and downstream to genes (approximately 30 %; Fig. 2, Table S1). The most frequent base change was C → T ($n = 690$), followed by G → A ($n = 632$), A → G ($n = 493$), and T → C ($n = 470$) base changes (Fig. 2). We note that C → T transitions are common signatures of pyrimidine dimer repair after UV exposure [45]. Our data suggest that *C. reinhardtii* also follows this trend. However, the ratio of C → T transitions introduced compared to other mutation classes likely depends on the time spent in the dark to prevent photoreactivation [46–48] and the UV exposure duration (multiple nucleotide track polymorphisms) and intensity (double-strand breaks, insertions and deletions) in the experimental conditions.

Notably, 45 genes had 'high-impact' mutations (Table S1, Fig. 2C). These mutations, detected by SnpEff [24], were predicted to substantially influence the encoded protein's function. Here, 'high-impact' mutations comprised mutations predicted to substantially perturb the coding sequence or splicing regions of the gene, including missense, frameshift, splice site alteration, and deletion/insertion mutations.

3.2. CLiP mutant validation reveals convergent genetic routes to lipid accumulation

To experimentally validate whether the identified high-impact mutations could causally affect lipid accumulation, we tested mutant strains from the Chlamydomonas Library Project (CLiP) collection [49–52] carrying independent insertional mutations in corresponding genes. Of the 45 genes with high-impact mutations in H5, 33 had available CLiP knock-in mutants. These strains were obtained from http://www.Chlamycollection.org and screened for lipid production using BODIPY 505/515 fluorescence and flow cytometry (Table S2, Fig. 2). Six CLiP mutants (18 % of tested strains) exhibited significantly elevated lipid content compared to the parental CC-5325 strain ($p < 0.05$, two-tailed *t*-test; Table S2, Fig. 2), while 27 strains showed no change or decreased accumulation.

Strikingly, two of the six lipid-accumulating mutants carry insertions in genes directly connected to our proposed metabolic mechanism: 6-phosphofructokinase (PFK1) and S-malonyltransferase. The PFK1 CLiP mutant independently validates that disrupting this glycolytic regulator increases lipid content, even without the specific regulatory-domain frameshift found in H5. The S-malonyltransferase mutant provides orthogonal biochemical support: this enzyme normally consumes malonyl-CoA for protein malonylation; its disruption would preserve malonyl-CoA pools for fatty acid synthesis, consistent with the 8.31-fold malonate increase observed in H5 metabolomics. The convergence of independent mutations in PFK1 and malonate-utilizing enzymes—both phenocopying H5's lipid accumulation—provides strong genetic evidence that deregulated glycolysis and malonyl-CoA availability are rate-limiting factors for lipid production in *C. reinhardtii*.

Importantly, most tested mutations (27/33, 82 %) did not increase lipid content, demonstrating that the H5 phenotype results from specific metabolic disruptions rather than general stress or growth defects. These functional validation experiments establish PFK1 and malonate metabolism as the genetic foundation for H5's altered lipid phenotype, setting the stage for examining how these mutations reshape gene expression and metabolic flux at the transcriptional level.

3.3. Transcriptomes of H5 and CC-503 converge after nitrogen deprivation

We interrogated the transcriptomes of H5 compared to WT in nutrient-replete and nitrogen-deprived conditions to examine differences in their transcriptomes regarding metabolic regulation and to test whether H5 displays a normal nitrogen-deprivation response (Table S3). Transcriptomic sequencing (RNAseq) for CC-503 and H5 cultures in triplicates was performed at 0, 1, and 3 days of nitrogen starvation (see Table S3). Mid-log phase ($OD_{600} = 0.4$) cells were harvested for the Day 0 timepoint. To define the contributions of deprived and nutrient-replete states towards lipid accumulation in H5 and CC-503, transcriptome analyses were performed at zero, one, and three days post-inoculation in Cuffdiff [28] (Table S1). The differentially expressed genes (DEGs) were screened at false discovery rate (FDR) - corrected *p* values (i.e., q values) ≤ 0.05 (Table S3). At Day 0, 11,126 and 10,554 genes were expressed in CC-503 and H5 at FPKM >1.0. Of these expressed genes, 10,094 were shared between the two strains, 1032 were unique in CC-503, and 460 were unique in H5. Differentially expressed genes from Day 0 (starting point, non-starvation control) and Day 1 (deprived for 24H) comprised 1798 and 1727 upregulated transcripts and 1296 and 1602 down-^{regulated} transcripts.

On Day 3 (deprived for 72H), H5 showed a similar expression profile as CC-503, as only 213 genes were up-regulated and 276 genes were down-regulated (Fig. 3 and Table S3). Thus, H5 exhibits drastically different transcriptome profiles in nitrogen-replete conditions but has transcript expression patterns closer to CC-503 after nitrogen deprivation.

Significant DEGs (Table S3) were classified into functional groups as in Gargouri et al. 2015 [53]. Photosynthesis, TCA cycle, and carbon fixation pathway, as well as multiple key nutrient deficiency-responsive genes (e.g., NIT1, SUOX1, see Fig. 3C–D), were upregulated in H5 compared to CC-503 (Fig. 3, Table S3). Several enzymes with predicted high-impact mutations, including a glycerol kinase and a TAG lipase (Table S1), were found to have very high expression levels (Table S3). Forty-six out of 70 lipid metabolism genes were upregulated in H5. These genes were involved in fatty acid, phosphatidylglycerol (PG), and acetyl-CoA synthesis. Also, 40 out of 43 genes involved in photosynthesis were upregulated, including five dominant LHCII complex genes (Table S3). Two mitochondrial carbonic anhydrases (CAH4/5), a cyclin-dependent kinase, pherophorin, and two transporter genes (ABC and anion transporter) were among the top down-regulated genes

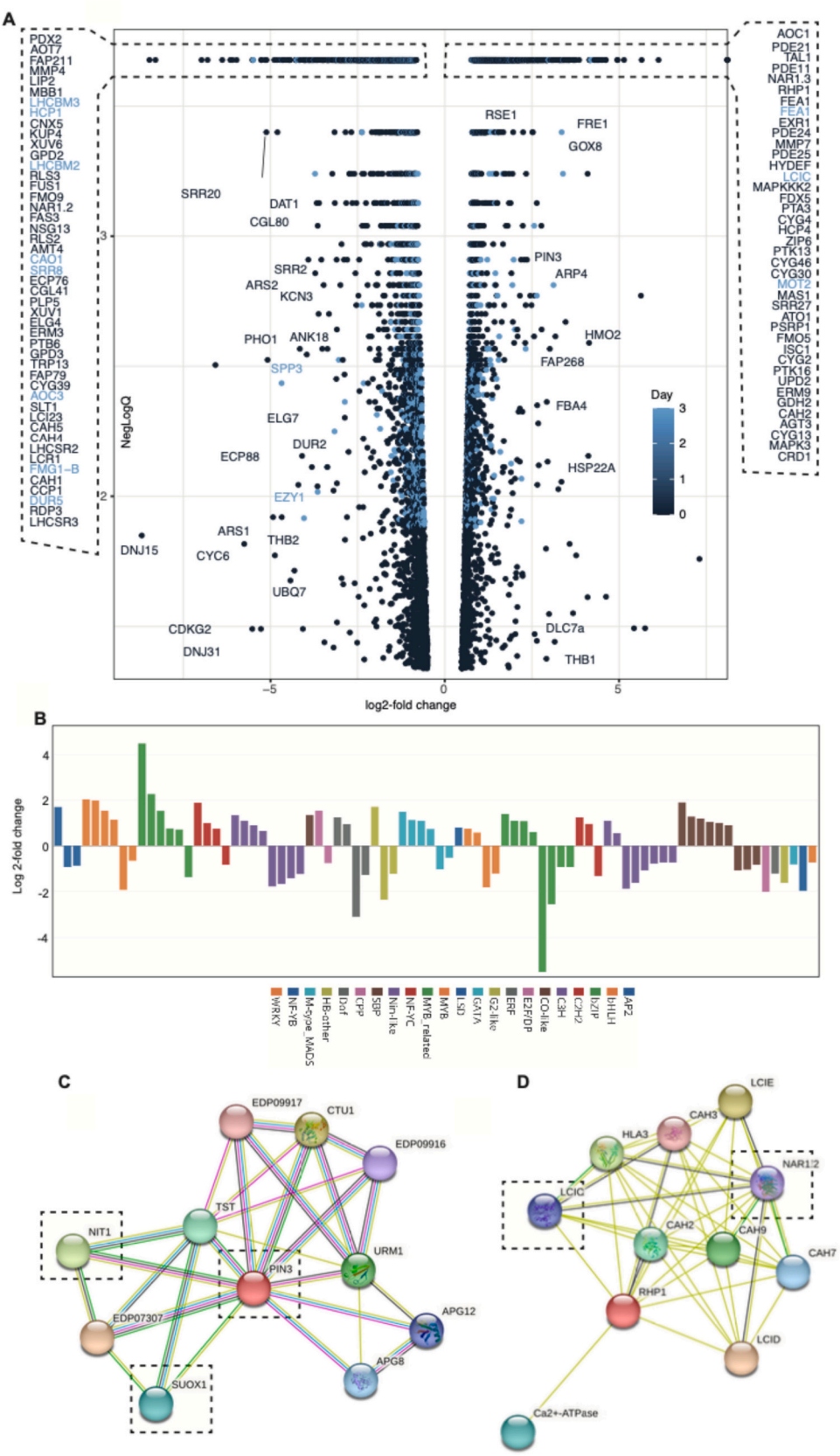

(caption on next page)

Fig. 3. Time-series transcriptomics resolves expression differences in H5 in nitrogen-replete and deprived conditions.
(A) DEGs between CC-503 and H5 during exponential growth (OD_{600} = 0.4) phase under nutrient-replete (Day 0) and nitrogen-deprived (Day 3) conditions (Table S3). Gene expression in mutants is displayed as a log 2-fold change in H5 compared to CC-503. Log 2-fold changes in each transcript (based on normalized FPKM values) against FDR-corrected *p* values (*q* values).
(B) Transcription factor landscape of H5 compared with CC-503 at Day 0. Many TFs with roles in cell growth and proliferation were upregulated in H5 (see Table S3).
(C) STRING (https://string-db.org/) functional association networks of highly-upregulated H5 genes. The central PIN3 is a parvullin homolog of *Arabidopsis* auxin transporters [87]. Red lines represent the presence of fusion evidence; green lines represent neighborhood evidence; blue lines represent co-occurrence evidence; purple lines represent experimental evidence; yellow lines represent text mining evidence; light blue lines represent database evidence, and black lines represent co-expression evidence (see also http://version10.string-db.org). SUOX1 and NIT1 are key enzymes in sulfur and nitrogen metabolism respectively, with SUOX1 oxidizing sulfite to sulfate and NIT1 reducing nitrate to nitrite in *Chlamydomonas*. Their dysregulation could trigger lipid accumulation through nutrient stress signaling and metabolic reallocation of energy resources.
(D) The carbonic anhydrase (CAH2, Cre04.g223050, log 2-fold change = 2.40148 $q = 0.000210344$, Table S3) was highly upregulated in H5. It is functionally linked (STRING) [108,109] to the low-carbon responsive proteins LCIC and LCID and a nitrate transporter (NAR). Its expression suggests that H5 has higher carbon and nitrogen assimilation rates than CC-503. (For interpretation of the references to color in this figure legend, the reader is referred to the web version of this article.)

(Table S3). These genes are likely involved in the dysregulated mitochondrial metabolism predicted in our metabolomic results (Fig. 4).

At Day 0, 21 transcripts expressed in CC-503 had no detectable expression in H5 (Table S3). Of these 21, three were annotated: HTR2, LCI1, and CGL16. The lack of high-temperature-responsive HTR2 suggests that H5 is less fit in the face of high-temperature stress. The low carbon-induced LCI1 protein [54] localizes to the plasma membrane and functions in active CO_2 uptake. Of the three annotated genes without detectable expression in H5, LCI1 had the highest expression in CC-503 at an FPKM of 48.8. The lack of LCI1 expression is likely related to the upregulation of the carbonic anhydrases (CAH2/3).

In contrast, the periplasmic CAH2 was significantly upregulated (Table S3). The CAH1 and CAH2 genes are both α-type periplasmic enzymes, although the CAH1 protein is reportedly not expressed in CC-503 [55]. Our results indicate that CAH1 the transcript is expressed in CC-503 (FPKM = 3006.8) despite a repeat insertion preceding the TSS. These data reveal a scenario where mitochondrial CAH activity is lowered in H5 concurrent with upregulated periplasmic CAH activity. The β-CAHs 4/5 proteins are usually not made unless CO_2 is limiting [56]. One interpretation of these results is that CO_2 is less of a limiting factor for H5, possibly due to the upregulation of CAH2. Still, the high levels of malonate (8.31×; $p = 8.5 \times 10–4$) observed in our metabolomics analyses suggest that mitochondrial function is at least partially impaired in H5 and would be expected to suppress the expression of β-CAHs 4/5 proteins. The accumulation of malonate directly links our genomic finding (deregulated PFK1) with the metabolic outcome (enhanced lipid biosynthesis). This PFK1-malonate-lipid axis represents the central mechanism driving H5's phenotype: unrestricted glycolysis generates excess pyruvate, which is carboxylated to malonate by the upregulated pyruvate carboxylase (PC3), providing both the carbon skeleton and reducing power for fatty acid synthesis.

The transcriptomic convergence of H5 and CC-503 under nitrogen deprivation demonstrated that H5 retained normal stress responses. However, under nutrient-replete conditions, H5 constitutively expressed stress-responsive genes—particularly those involved in glycolysis and nutrient acquisition—providing the transcriptional basis for examining downstream metabolic consequences.

3.4. Transcription factors (TFs) involved in lipid metabolism are significantly dysregulated in H5

We identified 23 putative transcription factors (TFs) during nutrient-replete ^{growth} in H5 from a total of 5316 DEGs (2832 upregulated genes and 2484 down-regulated genes) using the Plant Transcription Factor Database (PlantTFDB) v4.0 [57] as a reference (Fig. 3, Table S3). We identified regulators for 43 upregulated and 39 down-regulated genes (Table S3). Fatty acid and TAG accumulation have been shown to increase following the overexpression of Dof-type [58] and MYB [59] TF families in *C. reinhardtii*. Basic helix-loop-helix (bHLH) TFs are stress response, cell growth, and division regulators in plants; overexpression of bHLH TFs enhances biomass and lipid production in the microalga *Nannochloropsis salina* [60]. Another regulator of lipid metabolism and stress tolerance that can regulate multiple genes under stress and enhance biomass and lipid productivity in microalgae (e.g., *Nannochloropsis salina*, [61]) is the bZip transcription factor. Four genes from the bHLH family were upregulated in H5 (2.8–4.1 - fold increase), and six genes from the bZip family were upregulated (2.8–22-fold increase). These results outline a drastic shift in the transcription factor landscape of H5 predominantly centered around cell growth and lipid accumulation pathways. The upregulation of a majority of transcription factors from bZip and bHLH families in H5 may positively affect cell growth due to their roles in light signaling and cell development while maintaining increased lipid accumulation [60,61].

The widespread upregulation of growth-promoting transcription factors (bHLH, bZip) reinforced that H5's phenotype involved coordinated transcriptional reprogramming rather than isolated gene changes, directly supporting the enhanced glycolytic flux examined in metabolomic analyses.

3.5. H5 exhibits a cancer cell-like hypoxic nutrient deprivation response

Taken together with H5's increased lipid production, our results outline a scenario wherein H5 displays a high metabolic flux tumor cell-like phenotype [62–64]. The disruption of several environmentally-responsive genes (e.g., betaine lipids) [65–68] also suggests a decrease of H5 in natural conditions, mirroring the honing towards higher productivity through loss of non-essential reactions commonly seen in microbial engineering (i.e., synthetic microbial chassis) [69].

Although H5 cells display expression patterns indicating accelerated glycolysis, they also have expression patterns of hypoxic cells (Table S3). Hypoxia-responsive genes upregulated in H5 included the hydrogenase maturation factor (HYDEF, 9.3-fold increase, $q = 0.0002$, Table S3), ferredoxin (FDX5, 21.4-fold increase, $q = 0.0002$), hybrid cluster protein 4 (HCP4, 7.4-fold increase, $q = 0.0002$, Table S3), and malate synthase (MAS1). The HCP4 hub gene was one of the most highly upregulated genes. It is highly upregulated under anoxic conditions and orchestrates *C. reinhardtii*'s anoxic response [70]. The FDX5 is linked to sulfur deprivation and hypoxic response networks in *C. reinhardtii* [71]. Without sulfur, *C. reinhardtii* cells cannot produce photogenic oxygen because they cannot support the rapid turnover of the photosystem II (PSII) D1 protein [72]. They eventually become hypoxic and can produce hydrogen (H_2), among other biotechnologically interesting compounds [73,74]. The expression of FDX5 is controlled by sulfur deprivation independently of anoxia, and its expression is negatively regulated by nitric oxide (NO) [72]. The upregulation of multiple hypoxia-responsive transcripts (Table S3) indicates that H5 experiences a pseudo-hypoxia state.

Four guanylate cyclases (CYGx) were significantly upregulated in H5 during exponential growth (Table S3). We predicted a loss-of-function frameshift mutation in the putative NO-producing guanylate cyclase Cre02.g100500 H5. A soluble guanylate cyclase (CYG56) mediates negative signaling by ammonium on nitrate reductase expression in

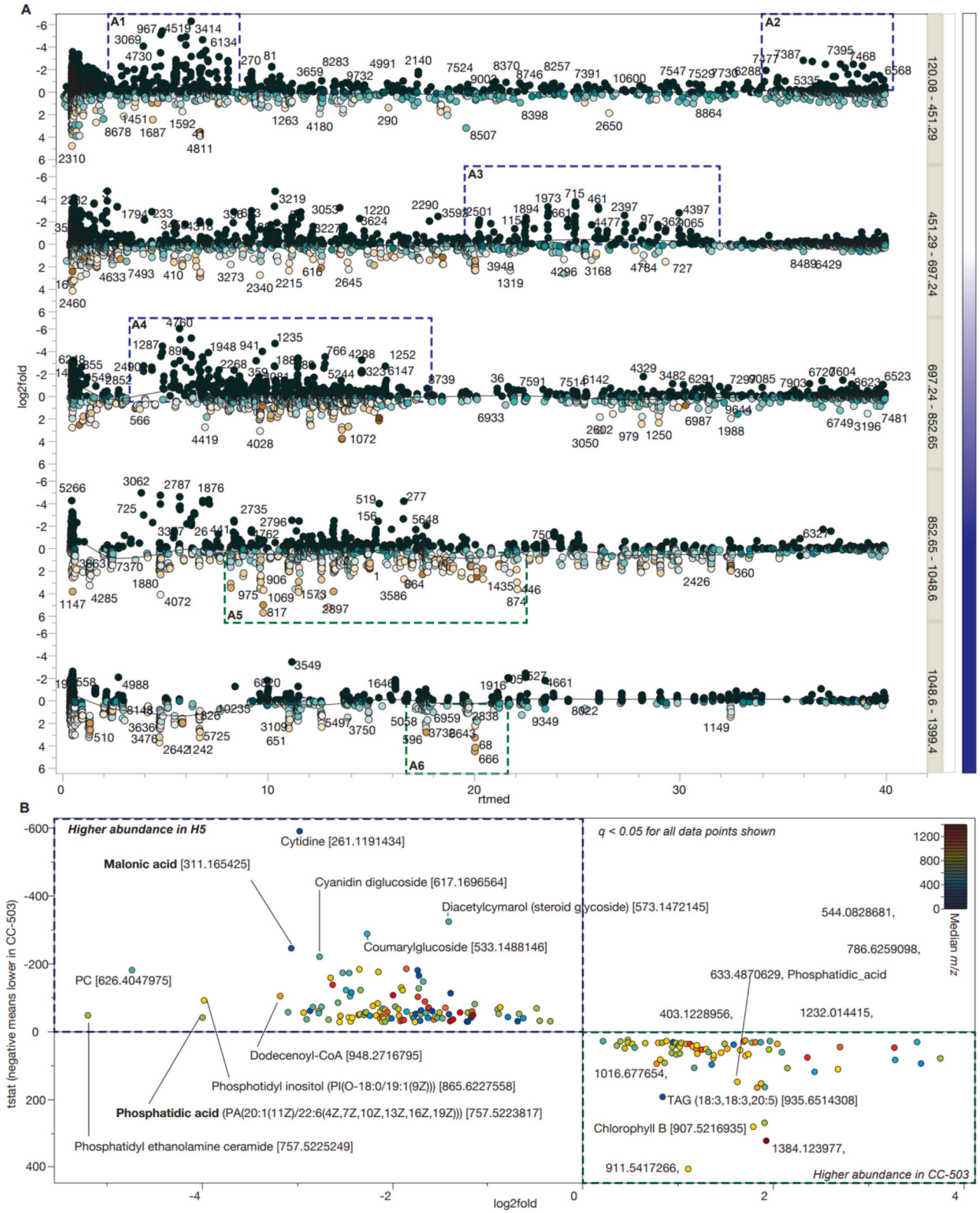

Fig. 4. Metabolites detected in LC/MS-QToF metabolomic experiments.
(A) Scatterplots are *m/z* bins showing comparative metabolomics for methanolic extracts of H5 vs. CC-503 at mid-log phase. This size bin shows an extensive array of various small, hydrophilic molecules accumulated in H5 (A1). Many free fatty acids were at higher concentrations in H5. In general, more compounds with later retention times in H5 indicate increased overall hydrophobicity of cell extracts. Accumulation of TAGs and free fatty acids in H5 explains the results described in (A2) and (A3; Glycerolipids, e.g., TAGs, increased in H5). Differential accumulation of H5 and CC-503 membrane lipids and their precursors in H5. High-impact mutations in enzymes in membrane lipid biosynthetic pathways are inferred to be responsible for the composition shift. Membrane lipids had lower diversity, while lipids containing saturated fatty acids were increased in H5 (A4–5). More high molecular weight (HMW) membrane lipids upregulated in CC-503 (A6).
(B) Compound abundance (y-axis) and log 2-fold change (x-axis) in H5 compared to CC-503.

C. reinhardtii [75]. The upregulation of the other four CYGs may be a compensatory mechanism for the disruption of Cre02.g100500. With the loss of NO production, FDX5 could be expected to increase in aerobic, sulfur-replete conditions, which we observed (Table S3). We investigated the possibility that the CYG Cre02.g100500 functions as an oxygen-sensing enzyme in *C. reinhardtii*; in this hypothesis, its ablation could explain the host of upregulated hypoxia-responsive genes in H5. However, the expression of Cre02.g100500 is extremely low in nutrient-replete conditions, precluding its possible role as a steady-state oxygen sensor. It is expressed only in nitrogen deprivation conditions in CC-503 (see https://conekt.sbs.ntu.edu.sg/), so its role in oxygen/nitrogen sensing is likely quite complex and dependent on multiple cofactors.

The copper deficiency responsive (CRD1) gene [76] was significantly upregulated in H5 in nitrogen-replete conditions (6.7-fold increase, $q = 0.0002$, Table S3). This gene is usually expressed at trace levels in CC-503 and is only upregulated in response to extreme copper or oxygen deprivation [76]. The RSE1 gene was also significantly upregulated in H5 at Day 0 (10.5-fold increase, $q = 0.00005$, Table S3). Although without annotated function, RSE1 is highly responsive to copper starvation [77]. This copper-responsive expression of RSE1 led the authors to conclude that RSE1 is a likely target for the copper-response regulator CRR1. The copper starvation and hypoxia responses partially overlap in *C. reinhardtii* [76]; this overlapping set of genes was seen among the broad array of anoxia-responsive genes upregulated in H5. Malate synthase (MAS1) was significantly upregulated in H5 in nitrogen-replete conditions (4.2-fold increase, $q = 0.0002$, Table S3), corresponding to the up-regulation of MAS1 in response to nitrogen starvation and TAG accumulation seen in previous studies [78].

The ammonium transporter RHP1 was significantly upregulated in H5 at Day 0 (4.4-fold increase, $q = 0.0002$, Table S3). Combined, these results outline a nutrient deprivation response in H5. Tumor cells experience constant nutrient demand, and cancer cells have what is commonly referred to as a "hungry" metabolic state [62–64]. Combined with the 8.31-fold malonate accumulation and accelerated glycolysis observed in metabolomics, H5 exhibits a "voracious" metabolic phenotype—constitutively acquiring and consuming nutrients. We use the term "voracious" to describe the H5 phenotype to avoid implying that it displays characteristics of starvation.

The constitutive activation of hypoxia and nutrient stress pathways in H5, combined with high metabolic flux, revealed an voracious metabolic state driving anabolic metabolism. This transcriptional phenotype provided mechanistic context for the downstream metabolic changes—particularly malonate accumulation and lipid remodeling—detailed in the following metabolomic analyses.

3.6. Expression of photosynthetic machinery is upregulated in H5

We observed transcriptomic evidence that photosynthesis is upregulated in H5. In *C. reinhardtii*, the non-photochemical quenching (NPQ) of chlorophyll fluorescence (qE) depends on light-induced accumulation of the LHCSR proteins, specifically LHCSR3 [79] In contrast, under the absence of LHCSR proteins, the structure of the PSII-LHCII supercomplexes changes in the HL-acclimated state to shift the distribution of the PSII antenna protein LHCBM5 towards the PSII core-enriched fraction B3 [80]. The primary LHCII complex forms from nine genes in *C. reinhardtii*, which group based on their sequence homology: Type I (LHCBM3, LHCBM4, LHCBM6, LHCBM8, LHCBM9), Type II (LHCBM5), Type III (LHCBM2, LHCBM7) and Type IV (LHCBM1). [81] In this study, five out of nine LHCII complex genes were upregulated in H5. This change is consistent with the alteration of the qE trigger mechanism from the LHCSR3 to the LHCII complex. The lack of LHCBM1 can reduce qE [82] and is needed to develop high NPQ as a partner for LHCSR3 [83].

A sulfite oxidase (SUOX1) was significantly upregulated in H5 in nitrogen-replete conditions. This enzyme recycles intracellular sulfur in *C. reinhardtii*. The increased accumulation of the SUOX transcript during sulfur deprivation implies that H5 breaks down intracellular sulfur molecules more rapidly than CC-503, again mirroring a nutrient deprivation response or 'hungry' state commonly seen in cancer cells [62–64]. The necessity may be from the higher turnover of the D1 protein of photosystem II (PSII). Eight of nine PSII (PsbX) proteins with significantly different expression in H5 were up-regulated (Table S3), indicating that photosynthesis is generally upregulated in H5.

Enhanced photosynthetic gene expression outlines an enhanced energy foundation supporting H5's increased metabolic flux. These transcriptional changes predicted increased carbon fixation capacity, which metabolomic profiling confirmed through elevated glycolytic intermediates and lipid precursors.

3.7. Transcriptomic reprogramming drives glycolytic flux towards lipid synthesis

Many glycolytic enzymes exhibited significantly upregulated transcript expression in H5. These correspond with the high-impact mutation disrupting the regulatory region of 6-phosphofructokinase (PFK1, Enzyme Commission (EC) 2.7.1.11, Table S1) and may be fundamentally responsible for increased glycolysis in H5. The PFK1 enzyme is typically allosterically inhibited by ATP in an energy-balancing central regulator of glycolysis [84]. PFK1 activation correlates with the anoxic and mitochondrial inhibition responses. The activation of PFK1 in response to mitochondrial inhibition or hypoxia promotes glycolysis and starch degradation, also known as the Pasteur effect [73,85,86].

The upregulation of glycolysis likely fuels increased lipid biosynthesis in H5. The significant upregulation of pyruvate decarboxylase (PDC3, 1.18579-fold increase, $q = 0.000210344$, Table S3) supports this hypothesis. The PDC3 enzyme decarboxylates pyruvate from glycolysis for entry into fatty acid synthesis, which would ultimately have the effect of increased availability of substrate for lipid accumulation. The other key data supporting carbon-increased funneling from glycolysis into fatty acid production was the high levels of malonate observed in our metabolomic experiments (8.31×; $p = 8.5 \times 10–4$). Other genes involved in starch and sucrose metabolism (Cre12.g488000, Cre06.g307150, Cre17.g721500, Cre12.g488050; KEGG pathway activation confidence score = 0.99712) and fructose and mannose metabolism (Cre10.g432900; KEGG score = 0.99755), as well as the pentose phosphate pathway (PPP; Cre03.g187450; KEGG score = 0.99265) were significantly upregulated in H5 in our KEGG analyses (Table S3). These metabolic enzymes normally have lower expression in nitrogen-limited conditions; their upregulation in H5 suggests intracellular nitrogen availability is not a primary factor in its enhanced lipid accumulation.

Five mitogen-activated protein kinases (MAPKs) were among the top 100 genes significantly upregulated in H5 ($q < 0.05$, Table S3). The function of this gene has yet to be experimentally verified, but other plant MAP kinases play roles in stress response and growth signaling. The numerous MAPKs upregulated in H5 suggest an influential role of these regulatory enzymes in the H5 phenotype. A 48 amino acid Parvulin-type peptidyl-prolyl cis-trans isomerase (PIN3, Cre07.g350400) was significantly upregulated in H5 in nitrogen-replete conditions (log 2-fold change = 2.18851, $q = 0.00123182$, Table S3). The PIN3 gene is a homolog of *Arabidopsis* auxin transporters. [87] Although the *C. reinhardtii* PIN3 is still uncharacterized, the mechanisms of auxin production in *C. reinhardtii* were elucidated [88]. The authors found that auxin production from L-tryptophan is mediated by an extracellular enzyme L-amino acid oxidase (LAO1) [88]. If the function of this parvullin-like gene is conserved, H5 may have increased auxin uptake leading to accelerated growth even when undergoing a pseudo-nutrient deprivation response. Our evidence suggests, however, that this would be a downstream effect from the accelerated glycolysis resulting from the deregulated 6-phosphofructokinase (see also Table S1 and Fig. 3).

Upregulated glycolytic genes, particularly PDC3 and pathways feeding into fatty acid synthesis, established the transcriptional framework for carbon flux redirection. This prediction was biochemically

validated through metabolomic detection of malonate and altered lipid profiles.

3.8. Metabolomics reveals upregulated glycolysis fueling the mutant lipidome

Metabolites from cell pellets of H5 and CC-503 from the exponential growth phase ($OD_{600} = 0.4$; i.e., nutrient-replete conditions) underwent microwave-assisted extraction with methanol [89,90]. Metabolites were loaded on a C-18 reverse phase column (Agilent, Santa Clara, CA, USA) and eluted using a semi-linear isopropanol gradient. Eluted compounds were interrogated with a QToF mass spectrometer (Fig. 4, Data S1). The resultant mass-to-charge ratio (m/z), ion abundance, and retention times were analyzed using the XCMS software suite (https://xcmsonline.scripps.edu) using nonlinear peak alignment, matching, and identification.

Overall, 7692 molecular features were detected in CC-503 and H5 methanolic extracts. Of these, 2196 had significant differences in abundance between the two strains ($p < 0.01$). Using XCMS metabolomics screening, we identified 5168 compounds correlating with the detected molecular features with differential abundance ($p < 0.00001$). Notably, we observed several metabolites with roles in lipid accumulation with differential abundance in CC-503 and the H5 mutant (Fig. 4). Compounds with putative signaling roles, including cyclo-pentadione and dihydrostilbene derivatives, were present at elevated levels or uniquely present in H5 (Fig. 4, Data S1). Pentadiones and stilbenes are hormone-like compounds that modulate energy metabolism [91,92]. We note that the unique presence of these molecules correlated with a high-impact mutation in a prostaglandin-F synthase (EC1.1.1.188, Data S1). Additionally, ethanamine, a nitric oxide donor [93], was more abundant in H5 (Data S1). The dysregulation of these molecules hints at disrupted hormonal signaling in H5.

We found 12 intermediate metabolites in the glycolipid and 11 in the glycerolipid desaturation pathways significantly dysregulated ($p < 0.05$) in H5. Malonate, an inhibitor of oxidative phosphorylation and promotor of glycolysis and cell proliferation, was 8.31× higher in H5 ($p = 8.5 \times 10^{-4}$) while chlorophyll *a* and *b* concentrations were 2.3- and 3.5-fold higher in CC-503 (Data S1 i.e., HPLC-MS metabolomics datasets). A gene coding for a glycerol kinase had a frameshift mutation in H5 (Table S1). As glycerol kinase catalyzes the phosphorylation of glycerol to form glycerol 3-phosphate, a component of glycerophospholipids, the loss-of-function mutation in a glycerol kinase would change the composition of lipids by decreasing the phospholipid population. A mutation in a lipase was also seen (Table S1). A loss-of-function mutation in this lipase would prevent the formation of product DAGs. Our metabolomics data shows a radical shift in all high-molecular-weight lipid populations, including TAGs, DAGs, and monoacylglycerols (MAGs). Many diacylglycerols (DAGs) were at lower concentrations in H5; however, the diversity of triacylglycerol classes increased. Nine TAG moieties were increased in H5, while five were decreased. Diacylglycerols (DAGs) were reduced in H5 compared to CC-503. The metabolomic and transcriptomic evidence suggests that TAG to DAG formation is perturbed in H5. Decreases in MGDG have coincided with increased TAG accumulation [94]. The higher diversity of TAGs may directly result from more energy and carbon allocation into TAG production after eliminating non-essential, conditional, standby metabolisms.

Betaine lipids are crucial for the adaptation to phosphate stress in some microalgae [95]. We observed four out of five detectable betaine lipids downregulated in H5 (Data S1). The lipids DGTA(18:1/22:4(10Z,13Z,16Z,19Z), DGTA(18:1/22:4(10Z,13Z,16Z,19Z)), DGTA(18:1/22:4(10Z,13Z,16Z,19Z)), and DGTS(16:0/16:0) were higher in CC-503, while DGTS(16:0/18:2(9Z,12Z)) was higher in H5 (Data S1). In addition to indicating a possible phosphate deficiency surplus, the absence of betaine lipids might be directly related to overall lipid accumulation in H5. Betaine is an efficient methyl donor known to increase nitrogen storage capacity and promote fat mobilization, as well as changing cellular fat content and composition [96]. Thus, the lack of betaine lipids in H5 likely has an influential role in its metabolism.

We observed very high levels of the nucleotide cytidine in H5 compared to CC-503 (Data S1). Abnormally high intracellular nucleotide levels and their metabolic demand are characteristic of tumor cells [97]; here, the increased cytidine appears to result from a block in its condensation with DAGs. The expression of a cytidine diphosphate diacylglycerol synthase (CDP-DAG) was down-regulated in H5 (Table S3, Fig. S3), corresponding with the absence of CDP-DAGs and high levels of intracellular cytidine (Data S1). These results suggest that the condensation of cytidine with phosphatic acid [98] is blocked in H5, which would be expected to reroute carbon flux into TAG production.

Malonate was also increased in H5 (8.31×; $p = 8.5 \times 10–4$), which indicates a strongly positive cellular energy balance. Malonate is an essential precursor and rate-limiting reactant in fatty acid biosynthesis; thus, its increased availability suggests a potential for higher lipid production. Excess malonate is toxic to mitochondria [99]. It inhibits succinate dehydrogenase, disrupting the electron transport chain driving oxidative phosphorylation, and diverting metabolism into glycolysis [100] Increased cell proliferation is also an effect of increased malonate; the high accumulation of this compound in H5 explains how H5 accumulates lipids while still proliferating at parental-like growth rates. Malonate accumulation is also observed in acute myeloid leukemia cells, corresponding to higher pyruvate carboxylase activity [101].

Metabolomic profiling validated transcriptional predictions: dysregulated PFK1 drove malonate accumulation (8.31-fold), which simultaneously inhibited mitochondrial function and fueled fatty acid synthesis. The dramatic lipid remodeling—increased TAG diversity, reduced DAGs and betaine lipids—demonstrated how genetic and transcriptional changes manifested as the observed biochemical phenotype (Fig. 5). This multi-layered metabolic reprogramming was potentially stabilized by the epigenetic changes examined next.

3.9. Global hypermethylation reveals stress-induced epigenetic reprogramming independent of gene expression

Whole-genome bisulfite sequencing of H5 revealed an unprecedented epigenetic phenomenon: significant hypermethylation in 100 % of analyzed genomic regions (90,603 regions, all $p < 0.05$) compared to the parental CC-503 strain. The mean methylation increase was 1.69 % (±3.33 % SD), affecting all 17 nuclear chromosomes (range: 1.33–2.20 % per chromosome, see Figs. 6, 7 and Data S2). The H5 strain exhibits genome-wide hypermethylation with 4.23 % mean methylation compared to 2.55 % in CC-503, representing a 1.66-fold increase in the mutant. Notably, our CC-503 control shows substantially higher baseline methylation than the ~0.4 % reported for *C. reinhardtii* [102], suggesting strain-specific or culture condition-dependent methylation variation.

Genome-wide hypermethylation was observed across all genomic contexts in H5 [promoters (mean +1.05 %), gene bodies (mean +1.03 %), and intergenic regions] with no hypomethylated regions detected. While the methylation coverage was sparse (median 2 sites per promoter, 4 sites per gene body), the uniformity of the hypermethylation signal across all 90,603 regions, combined with consistent technical replicates and the biological variability in methylation magnitude, strongly supports a scenario of global hypermethylation in H5. Chromosome 11 was the only chromosome showing strong hypermethylation at both telomeric regions, corresponding to drastically higher SNP density (Figs. 2 and 7), although we cannot causally link these changes to the H5 phenotype.

The hypermethylation in H5 cannot be explained by complete loss of known demethylases. All major DNA demethylation machinery (CMD1, UNG, TGD, ROS1) remains intact. However, three predicted N6-methyladenine demethylases (Cre09.g412350, Cre04.g217931, Cre14.g632791) carry MODIFIER variants in both H5 replicates, potentially

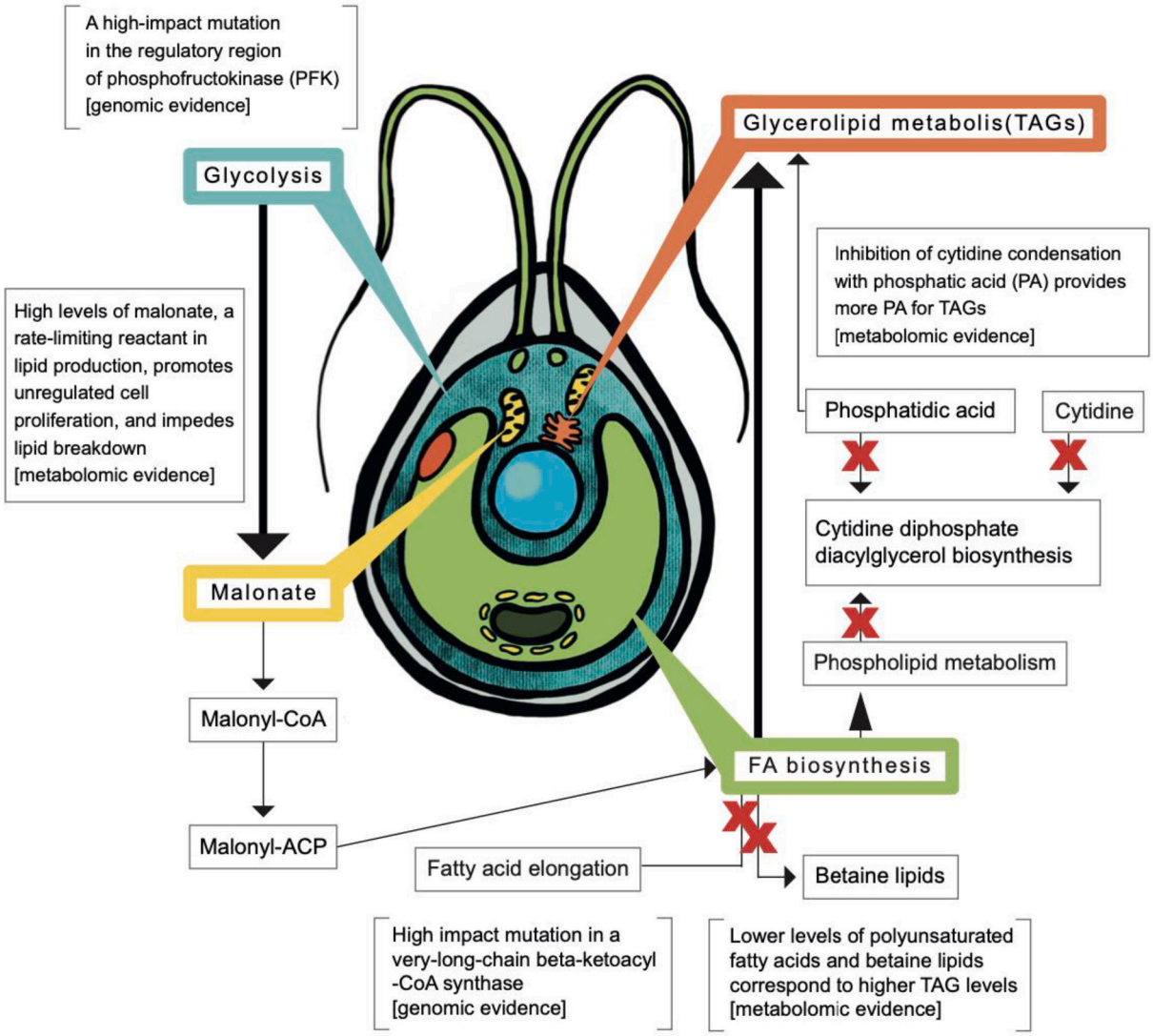

Fig. 5. Overview of multi-omics evidence explaining the H5 phenotype. The mutant strain H5 accumulates lipids during exponential phase growth through a combination of enhanced glycolysis and rerouting carbon from non-essential pathways to TAG and membrane lipid biosynthesis.

affecting regulatory regions. Additionally, N6-dMT_5 (Cre04.g224002), despite lacking mutations, shows significant downregulation (0.57-fold, FDR-corr. $p = 0.02$), suggesting reduced demethylation capacity may contribute to the hypermethylation phenotype.

The intersection of significantly differential methylation regions and differentially expressed genes (both FDR-corrected $p < 0.05$) comprised 2740 genes. Analysis of this intersection revealed a lack of methylation-expression correlation between H5 and CC-503, aligning with methylation-independent regulatory mechanisms observed across diverse microbial systems [103–105].

Neither promoter methylation changes (Pearson's $r = -0.025$, $p = 0.20$) nor gene body methylation changes (Pearson's $r = -0.019$, $p = 0.33$) showed any correlation with expression levels (Fig. 6). This lack of correlation persisted even when analyzing only well-covered genes (≥5 methylation sites, $n = 74$), indicating a genuine biological phenomenon rather than a coverage artifact. Expression of metabolic genes crucial for the H5 phenotype was uncorrelated with methylation status: alternative oxidase 1 (AOX1) was significantly upregulated (log2FC = +0.79, $p = 0.0004$) despite promoter and gene body hypermethylation (+0.6 % each), while glycolytic genes showed uniform hypermethylation but divergent expression responses (PFK1, FBA1, GAPDH upregulated; ENO1 downregulated). Among genes with cancer-like methylation patterns (body > promoter), only 49.5 % were upregulated, providing no predictive value for expression outcomes.

H5 exhibits 4-fold increased methylation compared to parental *C. reinhardtii* (Data S2; ~0.4 % baseline previously reported in Chlamydomonas, see Carballo et al. 2025 [102]), phenocopying the hypermethylated CMD1 mutant [106]. However, H5 lacks high-impact mutations in CMD1 or other characterized 5mC demethylases, though reduced N6-demethylase activity (through MODIFIER variants and transcriptional downregulation) combined with possible enhanced methyltransferase activity or disrupted uncharacterized pathways may contribute to the hypermethylation phenotype. Unlike the CMD1 mutant, which shows hypermethylation-dependent downregulation of photoprotective genes (e.g., LHCSR3) [106], H5 maintains expression of UV-response genes (e.g., AOX1) despite hypermethylation (Table S3, Fig. 6).

Analysis of 2740 genes with significant differential methylation and expression revealed no correlation (promoter r = −0.025, $p = 0.20$; gene body r = −0.019, $p = 0.33$), consistent with methylation-independent regulation in many other microorganisms [103,104]. The hypermethylation may represent a non-regulatory response to UV-induced genomic instability, potentially functioning in chromatin stabilization, transposon suppression, or DNA repair facilitation.

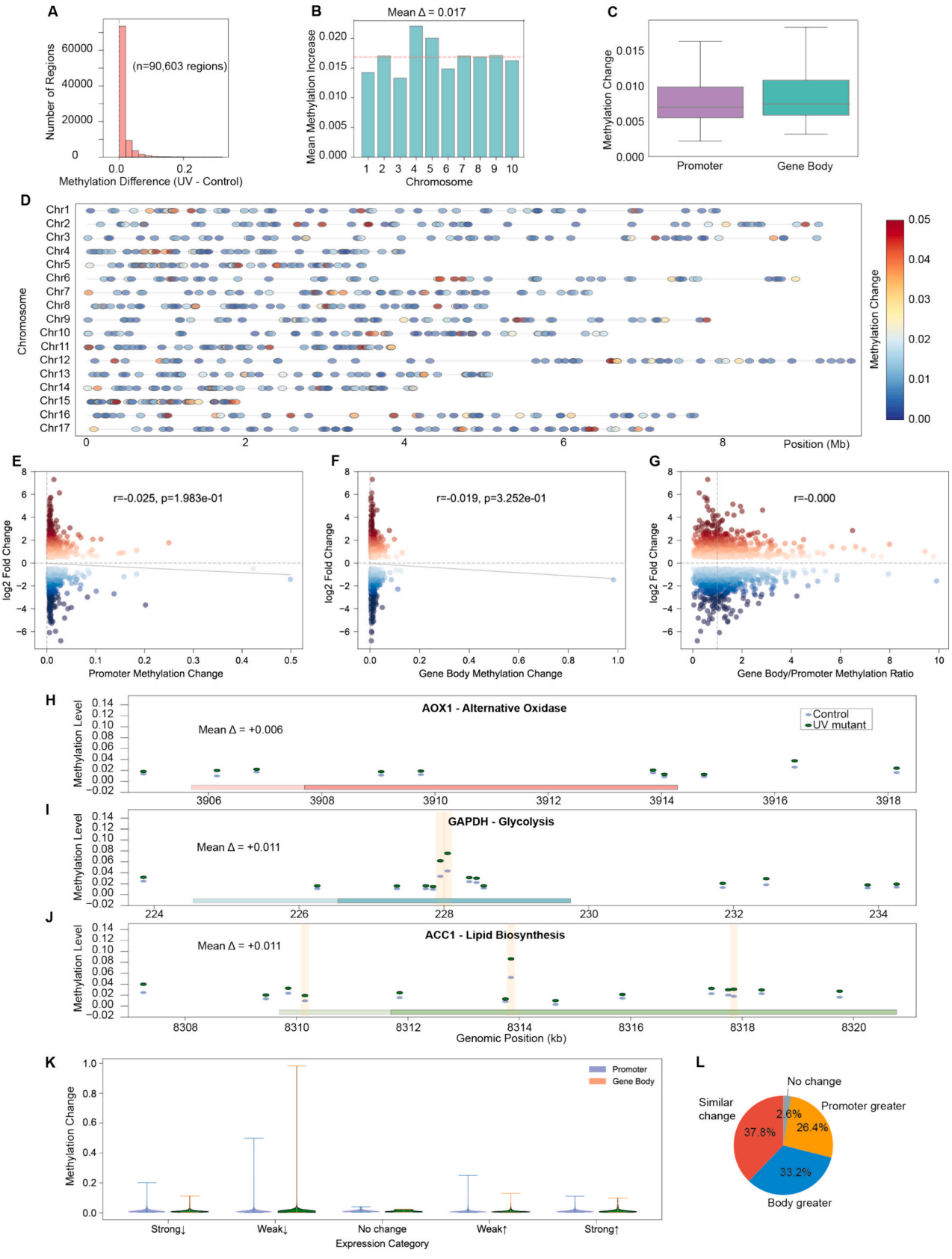

(caption on next page)

Fig. 6. Genome-wide hypermethylation with methylation-expression decoupling in H5.
(A) Distribution of methylation changes across 90,603 genomic regions showing universal hypermethylation in H5 versus CC-503. All regions show significant hypermethylation ($p < 0.05$, Fisher's Exact Test).
(B) Methylation changes across all 17 chromosomes. Bar chart showing mean methylation increase ($\Delta = 0.017$) with consistent hypermethylation across all chromosomes.
(C) Comparison of methylation changes between promoter and gene body regions. Box plots show similar median methylation increases in both regions (~0.007–0.010).
(D) Chromosome-wide methylation landscape. Heatmap showing methylation changes across all 17 chromosomes with position in megabases. Red indicates hypermethylation; blue indicates lower methylation change.
(E) Promoter methylation change versus gene expression. Scatter plot showing no correlation ($r = -0.025$, $p = 1.983e{-}01$) between promoter methylation changes and log2 fold-change expression ($n = 2740$ genes).
(F) Gene body methylation change versus expression. Scatter plot showing no correlation ($r = -0.019$, $p = 3.252e{-}01$) between gene body methylation changes and expression.
(G) Gene body/promoter methylation ratio versus expression. Scatter plot demonstrating absence of correlation ($r = 0.000$) between the methylation ratio and expression changes.
(H–J) Individual gene methylation tracks for key metabolic genes. (H) AOX1 - Alternative Oxidase, Mean $\Delta = +0.006$; (I) GAPDH - Glycolysis, Mean $\Delta = +0.011$; (J) ACC1 - Lipid Biosynthesis, Mean $\Delta = +0.011$. Blue dots show control methylation, orange dots show UV mutant. Green line indicates gene position.
(K) Methylation changes across expression categories. Bar plots showing mean methylation change for genes grouped by expression: Strong↓, Weak↓, No change, Weak↑, and Strong↑. Grey bars = promoter; pink bars = gene body. Error bars show standard deviation. No significant differences between categories.
(L) Distribution of methylation patterns. Pie chart showing proportions of genes with body greater than promoter (33.2 %), promoter greater than body (26.4 %), similar changes (37.8 %), and no change (2.6 %).
All methylation data from whole-genome bisulfite sequencing with >99.5 % conversion efficiency. Expression data from RNA-seq ($n = 3$ biological replicates for CC-503, n = 2 for H5). Statistical significance assessed by Fisher's Exact Test for methylation and DESeq2 for expression with FDR correction. (For interpretation of the references to color in this figure legend, the reader is referred to the web version of this article.)

The genome-wide hypermethylation in H5, while not directly regulating gene expression, may serve as a stabilizing mechanism for the complex multi-mutation phenotype. This epigenetic landscape could reinforce chromatin structure, suppress transposon mobility, and maintain genomic integrity following extensive UV-induced mutagenesis. The uniformity of hypermethylation across all chromosomes suggests a global cellular response rather than targeted regulatory changes, distinguishing H5's epigenetic reprogramming from typical stress-responsive methylation patterns. Together with the genetic, transcriptomic, and metabolomic alterations, this epigenetic remodeling completes the molecular portrait of H5's stable, high-productivity phenotype. Ultimately, we report a coordinated transformation spanning multiple regulatory layers that collectively bypass the traditional growth-lipid tradeoff.

4. Conclusions

This multi-omics analysis of the high-lipid *C. reinhardtii* mutant H5 reveals how the growth-lipid tradeoff can be overcome through coordinated metabolic reprogramming centered on deregulated glycolysis and malonyl-CoA metabolism. Whole-genome sequencing identified 45 high-impact mutations, with a frameshift in the regulatory domain of 6-phosphofructokinase (PFK1) emerging as a key driver. CLiP mutant screening independently validated this mechanism: mutations in PFK1 and S-malonyltransferase—both affecting malonyl-CoA availability—phenocopied H5's lipid accumulation, while mutations in mitochondrial transporters and phosphate metabolism genes indicate coordinated glycolytic and mitochondrial rewiring. These convergent genetic lesions demonstrate that malonyl-CoA availability is rate-limiting for lipid synthesis in *C. reinhardtii*.

Transcriptomics revealed constitutive expression of stress-responsive genes under nutrient-replete conditions, creating a "voracious" cellular state that drives anabolic metabolism. Metabolomics showed 8.31-fold malonate accumulation ($p = 8.5 \times 10^{-4}$), extensive lipidome remodeling, and depleted phospholipid intermediates. Malonate accumulation both inhibits mitochondrial respiration and provides precursors for fatty acid synthesis, enabling lipid accumulation without a growth penalty. Genome-wide hypermethylation (1.66-fold increase) may stabilize the multi-mutation phenotype, although methylation changes were uncoupled from gene expression. Convergent evidence from genetics, transcriptomics, metabolomics, and CLiP validation strongly supports deregulated glycolytic flux as the mechanistic basis for H5's phenotype.

H5 exemplifies a "cancer-like" metabolic strategy—upregulated glycolysis, constitutive stress signaling, altered mitochondrial function, and epigenetic reprogramming—that maximizes productivity in industrial cultivation. Multiple independent genetic routes converge on the PFK1-malonyl-CoA-lipid axis, highlighting a metabolic vulnerability that can be exploited through diverse engineering strategies.

These findings demonstrate that UV mutagenesis and selection can generate solutions inaccessible to rational design. The PFK1 regulatory-domain-specific frameshift—preserving catalytic activity while abolishing feedback inhibition—represents a modification difficult to achieve without extensive structure-function characterization. Rational engineering targets identified include the PFK1 regulatory domain, S-malonyltransferase, and CDP-DAG synthase, though combinatorial strategies may be required to fully recapitulate H5's productivity.

By showing how coordinated mutations in glycolytic regulation, malonate metabolism, and lipid partitioning enable sustained high-lipid production, this work provides mechanistic insights and practical targets for engineering commercially viable microalgal strains. The UV mutagenesis and FACS-based selection strategy offers a generalizable approach to accelerate development of high-lipid strains across diverse microalgae.

CRediT authorship contribution statement

David R. Nelson: Writing – review & editing, Writing – original draft, Visualization, Software, Investigation, Formal analysis, Data curation, Conceptualization. **Amphun Chaiboonchoe:** Writing – review & editing, Writing – original draft, Visualization, Software, Methodology, Formal analysis, Data curation, Conceptualization. **Weiqi Fu:** Writing – review & editing, Writing – original draft, Validation, Methodology, Investigation, Formal analysis, Conceptualization. **Basel Khraiwesh:** Writing – review & editing, Writing – original draft, Visualization, Software, Investigation, Formal analysis. **Bushra Dohai:** Writing – review & editing, Writing – original draft, Visualization, Software, Investigation, Formal analysis. **Ashish Jaiswal:** Writing – review & editing, Writing – original draft, Visualization, Software, Investigation, Formal analysis. **Dina Al-Khairy:** Writing – review & editing, Writing – original draft, Investigation, Formal analysis. **Alexandra Mystikou:** Writing – review & editing, Writing – original draft, Investigation. **Latifa Al Nahyan:** Writing – review & editing, Writing – original draft, Investigation. **Amnah Salem Alzahmi:** Writing – review & editing, Writing – original draft, Investigation, Formal analysis.

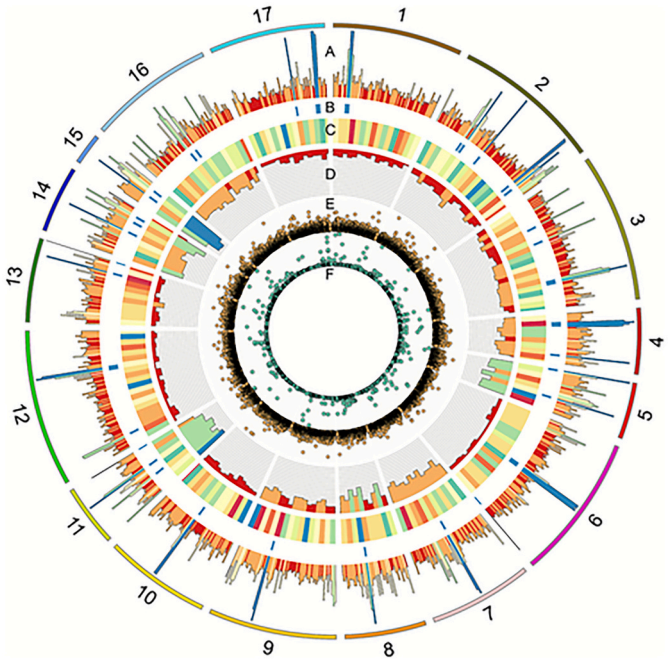

Fig. 7. Multi-omics Circos plot of epigenomic changes in UV-exposed *Chlamydomonas reinhardtii*.
Circular ideogram represents the 17 nuclear chromosomes of *C. reinhardtii*. Tick marks indicate genomic positions at 1 Mb (minor ticks) and 5 Mb intervals (major labeled ticks). Colorscale ranges are displayed in Brewer palettes [110]. Data tracks display multi-omics measurements in genomic windows, arranged from outer to inner radius:
(A) Methylation histogram ($r = 0.99$–$0.77r$, orientation: outward): CG methylation levels binned across the genome, displayed as histogram bars extending outward from the ideogram. Bar height represents methylation proportion (0–5 % scale). Colors follow a 5-class spectral diverging palette (spectral-5-div): lowest methylation (<1 %) in blue (spectral-5-div-1), increasing through intermediate levels (1–2 %, 2–3 %, 3–4 %) to highest methylation (≥4 %) in red (spectral-5-div-5).
(B) Methylation hotspots ($r = 0.76$–$0.72r$): Tile track showing discrete regions with elevated methylation (≥4 %). Each tile represents a contiguous genomic interval meeting the hotspot threshold. Tiles colored in spectral-5-div-4 with spectral-5-div-5 borders to distinguish individual hotspot regions.
(C) Gene expression heatmap ($r = 0.70$–$0.62r$): Log2 fold-change values for differentially expressed genes in binned genomic windows, displayed as a continuous heatmap. Scale ranges from −0.8 (downregulated) to +0.8 (upregulated) with 9-class spectral diverging color scheme (spectral-9-div). Blue colors (spectral-9-div-1 through −4) represent downregulation, neutral expression near zero shown in yellow-green (spectral-9-div-5), and upregulation in orange-red (spectral-9-div-6 through −9). Breakpoints: <−0.6, −0.6 to −0.4, −0.4 to −0.2, −0.2 to −0.05, −0.05 to +0.05, +0.05 to +0.2, +0.2 to +0.4, +0.4 to +0.6, ≥0.6.
(D) SNP density histogram ($r = 0.60$–$0.45r$, orientation: inward): SNP counts per genomic window, displayed as histogram bars extending inward towards the center. Bar height represents SNP count (0–40 per window scale). Colors follow 4-class spectral palette: low density (<10 SNPs) in blue (spectral-5-div-1), increasing through medium density (10–20, 20–30) to high density (≥30 SNPs) in red (spectral-5-div-5). Light grey background with horizontal grid lines at 0.05r spacing.
(E) Gene scatter plot ($r = 0.43$–$0.33r$): Annotated gene positions from genome GFF3 file ($n = 17{,}743$). Each circle represents one gene, with radial position (y-axis) indicating gene length (0–50 kb scale). Circle size: 8 pixels, colored in spectral-9-div-3 (blue-green). Light grey background indicates track boundaries.
(F) Repeat scatter plot ($r = 0.32$–$0.22r$): Annotated repeat element positions from genome GFF3 biological_region features ($n = 1459$). Each circle represents one repeat element, with radial position indicating element length (0–50 kb scale). Circle size: 9 pixels, colored in spectral-9-div-8 (orange-red). Light grey background indicates track boundaries.
All color schemes use ColorBrewer spectral diverging palettes. Genomic positions extracted from *C. reinhardtii* reference genome annotation (chlamy.gff3). Gap between chromosomes 17 and 1 (spacing = 0.3r) provided for figure panel labeling. (For interpretation of the references to color in this figure legend, the reader is referred to the web version of this article.)

Layanne Nayfeh: Writing – review & editing, Writing – original draft, Investigation. **Sarah Daakour:** Writing – review & editing, Writing – original draft, Investigation, Formal analysis. **Matthew J. O'Connor:** Writing – review & editing, Writing – original draft, Conceptualization. **Mehar Sultana:** Writing – review & editing, Writing – original draft, Investigation. **Khaled M. Hazzouri:** Writing – review & editing, Writing – original draft, Software, Investigation, Formal analysis. **Jean-Claude Twizere:** Writing – review & editing, Writing – original draft. **Kourosh Salehi-Ashtiani:** Writing – review & editing, Writing – original draft, Supervision, Resources, Methodology, Investigation, Formal analysis, Conceptualization.

Declaration of Generative AI and AI-assisted technologies in the writing process

During the preparation of this work the authors used OpenAI's ChatGPT to improve readability and language of the work and not to replace key authoring tasks such as producing scientific, pedagogic, or medical insights, drawing scientific conclusions, or providing clinical recommendations. We applied the technology with human oversight and control, and all work was reviewed and carefully edited. We acknowledge that we are ultimately responsible and accountable for the contents of the work.

Declaration of competing interest

The authors declare no competing financial interests.

Acknowledgements

Financial support for this work was provided by New York University Abu Dhabi Faculty Research Funds (AD060) and by the NYUAD Research Institute grant (G1205-1205i). We thank Marc Arnoux and the CGSB Sequencing Core for high throughput sequencing, Nizar Drou and CGSB Bioinformatics Core for raw RNAseq data processing, Sujirat Nelson for the algal cell illustration, and NYUAD High-Performance

Computing and Core Technology Platforms for their resources and logistical support.

Appendix A. Supplementary data

Supplementary data to this article can be found online at https://doi.org/10.1016/j.algal.2025.104479.

Data availability

Supplementary data are available at Zenodo DOI: https://doi.org/10.5281/zenodo.14525303. The repository includes raw metabolomics data—total ion chromatograms (TICs) and extracted ion chromatograms (EICs)—as well as all supplementary datasets associated with the analyses. Raw sequencing data for the omics experiments are deposited in the NCBI SRA under the following Bioprojects: PRJNA1216387 (genomic reads for variant analysis), PRJNA1216608 and PRJNA389185 (RNA-seq for nitrogen starvation transcriptomics), and PRJNA1158323 (whole-genome bisulfite sequencing for epigenomics).

References

[1] S.K. Sharma, D.R. Nelson, R. Abdrabu, B. Khraiwesh, K. Jijakli, M. Arnoux, M. J. O'Connor, T. Bahmani, H. Cai, S. Khapli, An integrative raman microscopy-based workflow for rapid in situ analysis of microalgal lipid bodies, Biotechnol. Biofuels 8 (1) (2015) 164.
[2] R. Abdrabu, S.K. Sharma, B. Khraiwesh, K. Jijakli, D.R. Nelson, A. Alzahmi, J. Koussa, M. Sultana, S. Khapli, R. Jagannathan, et al., Single-cell characterization of microalgal lipid contents with confocal raman microscopy, in: F.-G. Tseng, T.S. Santra (Eds.), Essentials of Single-cell Analysis: Concepts, Applications and Future Prospects, Springer Berlin Heidelberg, Berlin, Heidelberg, 2016, pp. 363–382.
[3] P. Spolaore, C. Joannis-Cassan, E. Duran, A. Isambert, Commercial applications of microalgae, J. Biosci. Bioeng. 101 (2) (2006) 87–96.
[4] R.K. Saini, G.A. Ravishankar, Y.S. Keum, Microalgae and thraustochytrids are sustainable sources of vegan epa and dha with commercial feasibility, Indian J. Microbiol. 63 (1) (2023) 155–158.
[5] P. Ma, X. Li, B. Wu, Z. Liu, Z. Li, X. Sun, L. Zhou, M. Du, Evaluating growth and nitrogen and phosphorus removal of four microalgae in different nutrient concentrations, Biology (Basel) 14 (9) (2025).
[6] C. Arenas Colarte, I. Balic, O. Diaz, A.A. Moreno, M.J. Amenabar, T. Bruna Larenas, N. Caro Fuentes, High-value bioactive molecules extracted from microalgae, Microorganisms 13 (9) (2025).
[7] J. Popp, Z. Lakner, M. Harangi-Rákos, M. Fári, The effect of bioenergy expansion: Food, energy, and environment, Renew. Sustain. Energy Rev. 32 (2014) 559–578.
[8] G. Brennan, S. Collins, Growth responses of a green alga to multiple environmental drivers, Nat Clim Change 5 (9) (2015) 892+.
[9] K.M. Carlson, R. Heilmayr, H.K. Gibbs, P. Noojipady, D.N. Burns, D.C. Morton, N. F. Walker, G.D. Paoli, C. Kremen, Effect of oil palm sustainability certification on deforestation and fire in indonesia, Proc. Natl. Acad. Sci. U. S. A. 115 (1) (2018) 121–126.
[10] D.L.A. Gaveau, B. Locatelli, M.A. Salim, Husnayaen, T. Manurung, A. Descals, A. Angelsen, E. Meijaard, D. Sheil, Slowing deforestation in Indonesia follows declining oil palm expansion and lower oil prices, PLoS One 17 (3) (2022) e0266178.
[11] D.R. Nelson, B. Khraiwesh, W. Fu, S. Alseekh, A. Jaiswal, A. Chaiboonchoe, K. M. Hazzouri, M.J. O'Connor, G.L. Butterfoss, N. Drou, et al., The genome and phenome of the green alga Chloroidium sp. Utex 3007 reveal adaptive traits for desert acclimatization, Elife 6 (2017).
[12] E.M. Ordway, R.L. Naylor, R.N. Nkongho, E.F. Lambin, Oil palm expansion and deforestation in southwest cameroon associated with proliferation of informal mills, Nat. Commun. 10 (1) (2019) 114.
[13] Z. Zhu, J. Sun, Y. Fa, X. Liu, P. Lindblad, Enhancing microalgal lipid accumulation for biofuel production, Front. Microbiol. 13 (2022) 1024441.
[14] R.H. Wijffels, O. Kruse, K.J. Hellingwerf, Potential of industrial biotechnology with cyanobacteria and eukaryotic microalgae, Curr. Opin. Biotechnol. 24 (3) (2013) 405–413.
[15] M. Siaut, S. Cuiné, C. Cagnon, B. Fessler, M. Nguyen, P. Carrier, A. Beyly, F. Beisson, C. Triantaphylidès, Y. Li-Beisson, Oil accumulation in the model green alga Chlamydomonas reinhardtii: Characterization, variability between common laboratory strains and relationship with starch reserves, BMC Biotechnol. 11 (1) (2011) 7.
[16] M. Kallau, H. Yang, Quantification of the total lipids in three aquaculture microalgae using bodipy™ 505/515 stain and flow cytometry, J. World Aquacult. Soc. 56 (3) (2025).
[17] D. Xu, Z. Gao, F. Li, X. Fan, X. Zhang, N. Ye, S. Mou, C. Liang, D. Li, Detection and quantitation of lipid in the microalga tetraselmis subcordiformis (wille) butcher with bodipy 505/515 staining, Bioresour. Technol. 127 (2013) 386–390.
[18] J. Rumin, H. Bonnefond, B. Saint-Jean, C. Rouxel, T. Sciandra, O. Bernard, J.-P. Cadoret, G. Bougaran, Bodipy 505/515 as a sensitive probe for quantification of neutral lipids in microalgae, Algal Res. 10 (2015) 80–87.
[19] J. Rumin, H. Bonnefond, B. Saint-Jean, C. Rouxel, A. Sciandra, O. Bernard, J. P. Cadoret, G. Bougaran, The use of fluorescent nile red and bodipy for lipid measurement in microalgae, Biotechnol. Biofuels 8 (2015) 42.
[20] L. Brennan, A. Blanco Fernández, A.S. Mostaert, P. Owende, Enhancement of bodipy505/515 lipid fluorescence method for applications in biofuel-directed microalgae production, J. Microbiol. Methods 90 (2) (2012) 137–143.
[21] D.S. Gorman, R.P. Levine, Cytochrome f and plastocyanin: their sequence in the photosynthetic electron transport chain of Chlamydomonas reinhardi, Proc. Natl. Acad. Sci. U. S. A. 54 (6) (1965) 1665–1669.
[22] B. Langmead, C. Trapnell, M. Pop, S.L. Salzberg, Ultrafast and memory-efficient alignment of short DNA sequences to the human genome, Genome Biol. 10 (3) (2009) R25.
[23] H. Li, B. Handsaker, A. Wysoker, T. Fennell, J. Ruan, N. Homer, G. Marth, G. Abecasis, R. Durbin, The sequence alignment/map format and samtools, Bioinformatics 25 (16) (2009) 2078–2079.
[24] P. Cingolani, A. Platts, L. Wang le, M. Coon, T. Nguyen, L. Wang, S.J. Land, X. Lu, D.M. Ruden, A program for annotating and predicting the effects of single nucleotide polymorphisms, snpeff: Snps in the genome of *Drosophila melanogaster* strain w1118; iso-2; iso-3, Fly (Austin) 6 (2) (2012) 80–92.
[25] B. Langmead, S.L. Salzberg, Fast gapped-read alignment with bowtie 2, Nat. Methods 9 (4) (2012) 357–359.
[26] C. Robert, M. Watson, Errors in rna-seq quantification affect genes of relevance to human disease, Genome Biol. 16 (1) (2015) 177.
[27] Z.T. Wang, N. Ullrich, S. Joo, S. Waffenschmidt, U. Goodenough, Algal lipid bodies: stress induction, purification, and biochemical characterization in wild-type and starchless *Chlamydomonas reinhardtii*, Eukaryot. Cell 8 (12) (2009) 1856–1868.
[28] C. Trapnell, D.G. Hendrickson, M. Sauvageau, L. Goff, J.L. Rinn, L. Pachter, Differential analysis of gene regulation at transcript resolution with rna-seq, Nat. Biotechnol. 31 (1) (2013) 46–53.
[29] S. Maere, K. Heymans, M. Kuiper, Bingo: a cytoscape plugin to assess overrepresentation of gene ontology categories in biological networks, Bioinformatics 21 (16) (2005) 3448–3449.
[30] Y.H. Benjamini, Yosef: controlling the false discovery rate: a practical and powerful approach to multiple testing, J Roy Statist Soc Ser 1 (1995) 289–300.
[31] A. Chaiboonchoe, B.S. Dohai, H. Cai, D.R. Nelson, K. Jijakli, K. Salehi-Ashtiani, Microalgal metabolic network model refinement through high-throughput functional metabolic profiling, Front. Bioeng. Biotechnol. 2 (2014) 68.
[32] D. Lopez, D. Casero, S.J. Cokus, S.S. Merchant, M. Pellegrini, Algal functional annotation tool: a web-based analysis suite to functionally interpret large gene lists using integrated annotation and expression data, BMC Bioinformatics 12 (1) (2011) 282.
[33] J.M. Castro-Perez, J. Kamphorst, J. DeGroot, F. Lafeber, J. Goshawk, K. Yu, J. P. Shockcor, R.J. Vreeken, T. Hankemeier, Comprehensive lc− mse lipidomic analysis using a shotgun approach and its application to biomarker detection and identification in osteoarthritis patients, J. Proteome Res. 9 (5) (2010) 2377–2389.
[34] H. Gowda, J. Ivanisevic, C.H. Johnson, M.E. Kurczy, H.P. Benton, D. Rinehart, T. Nguyen, J. Ray, J. Kuehl, B. Arevalo, et al., Interactive xcms online: simplifying advanced metabolomic data processing and subsequent statistical analyses, Anal. Chem. 86 (14) (2014) 6931–6939.
[35] R. Tautenhahn, G.J. Patti, D. Rinehart, G. Siuzdak, Xcms online: a web-based platform to process untargeted metabolomic data, Anal. Chem. 84 (11) (2012) 5035–5039.
[36] N.G. Mahieu, J.L. Genenbacher, G.J. Patti, A roadmap for the xcms family of software solutions in metabolomics, Curr. Opin. Chem. Biol. 30 (2016) 87–93.
[37] T. Huan, E.M. Forsberg, D. Rinehart, C.H. Johnson, J. Ivanisevic, H.P. Benton, M. Fang, A. Aisporna, B. Hilmers, F.L. Poole, et al., Systems biology guided by xcms online metabolomics, Nat. Methods 14 (5) (2017) 461–462.
[38] D.S. Wishart, D. Tzur, C. Knox, R. Eisner, A.C. Guo, N. Young, D. Cheng, K. Jewell, D. Arndt, S. Sawhney, Hmdb: the human metabolome database, Nucleic Acids Res. 35 (Suppl. 1) (2007) D521–D526.
[39] R. Tokutsu, K. Fujimura-Kamada, T. Yamasaki, K. Okajima, J. Minagawa, Uv-a/b radiation rapidly activates photoprotective mechanisms in *Chlamydomonas reinhardtii*, Plant Physiol. 185 (4) (2021) 1894–1902.
[40] S.Q. Kulp, H.G. Griggs, Photoreactivation of lethal damage and damage leading to chromatid deletions induced in g1 phase hamster x Xenopus hybrid cells by uv, Photochem. Photobiol. 50 (2) (1989) 185–191.
[41] D.D. Levy, A.D. Magee, M.M. Seidman, Single nucleotide positions have proximal and distal influence on uv mutation hotspots and coldspots, J. Mol. Biol. 258 (2) (1996) 251–260.
[42] M.F. Laughery, A.J. Brown, K.A. Bohm, S. Sivapragasam, H.S. Morris, M. Tchmola, A.D. Washington, D. Mitchell, S. Mather, E.P. Malc, et al., Atypical uv photoproducts induce non-canonical mutation classes associated with driver mutations in melanoma, Cell Rep. 33 (7) (2020) 108401.
[43] G.A. Fontana, H.L. Gahlon, Detection of uv-induced deletions in mitochondrial DNA, Methods Mol. Biol. 2615 (2023) 281–292.
[44] S.S. Merchant, S.E. Prochnik, O. Vallon, E.H. Harris, S.J. Karpowicz, G.B. Witman, A. Terry, A. Salamov, L.K. Fritz-Laylin, L. Maréchal-Drouard, et al., The Chlamydomonas genome reveals the evolution of key animal and plant functions, Science 318 (5848) (2007) 245–250.
[45] J.-S. Taylor, Deamination of c-containing cyclobutane pyrimidine dimers and its role in c to t and cc to tt signature mutations caused by uv light, in: R. Improta,

T. Douki (Eds.), DNA Photodamage: From Light Absorption to Cellular Responses and Skin Cancer, The Royal Society of Chemistry, 2021, p. 0.
[46] L. Ryznar, V. Drasil, Photoreactivation in Chlamydomonas reinhardi dangeard, Folia Microbiol. (Praha) 12 (6) (1967) 524–528.
[47] J.L. Petersen, P.J. Ronan, Critical role of 7,8-didemethyl-8-hydroxy-5-deazariboflavin for photoreactivation in *Chlamydomonas reinhardtii*, J. Biol. Chem. 285 (42) (2010) 32467–32475.
[48] J.L. Cox, G.D. Small, Isolation of a photoreactivation-deficient mutant of Chlamydomonas, Mutat. Res. 146 (3) (1985) 249–255.
[49] R.E. Jinkerson, M.C. Jonikas, Molecular techniques to interrogate and edit the Chlamydomonas nuclear genome, Plant J. 82 (3) (2015) 393–412.
[50] X. Li, M.C. Jonikas, High-throughput genetics strategies for identifying new components of lipid metabolism in the green alga *Chlamydomonas reinhardtii*, Subcell. Biochem. 86 (2016) 223–247.
[51] X. Li, R. Zhang, W. Patena, S.S. Gang, S.R. Blum, N. Ivanova, R. Yue, J. M. Robertson, P.A. Lefebvre, S.T. Fitz-Gibbon, et al., An indexed, mapped mutant library enables reverse genetics studies of biological processes in *Chlamydomonas reinhardtii*, Plant Cell 28 (2) (2016) 367–387.
[52] F. Fauser, J. Vilarrasa-Blasi, M. Onishi, S. Ramundo, W. Patena, M. Millican, J. Osaki, C. Philp, M. Nemeth, P.A. Salome, et al., Systematic characterization of gene function in the photosynthetic alga *Chlamydomonas reinhardtii*, Nat. Genet. 54 (5) (2022) 705–714.
[53] M. Gargouri, J.J. Park, F.O. Holguin, M.J. Kim, H.X. Wang, R.R. Deshpande, Y. Shachar-Hill, L.M. Hicks, D.R. Gang, Identification of regulatory network hubs that control lipid metabolism in *Chlamydomonas reinhardtii*, J. Exp. Bot. 66 (15) (2015) 4551–4566.
[54] A. Kono, M.H. Spalding, Lci1, a *Chlamydomonas reinhardtii* plasma membrane protein, functions in active co(2) uptake under low co(2), Plant J. 102 (6) (2020) 1127–1141.
[55] H. Fukuzawa, S. Fujiwara, A. Tachiki, S. Miyachi, Nucleotide sequences of two genes cah1 and cah2 which encode carbonic anhydrase polypeptides in *Chlamydomonas reinhardtii*, Nucleic Acids Res. 18 (21) (1990) 6441–6442.
[56] A.K. Rai, T. Chen, J.V. Moroney, Mitochondrial carbonic anhydrases are needed for optimal photosynthesis at low co2 levels in Chlamydomonas, Plant Physiol. 187 (3) (2021) 1387–1398.
[57] J. Jin, F. Tian, D.-C. Yang, Y.-Q. Meng, L. Kong, J. Luo, G. Gao, Planttfdb 4.0: toward a central hub for transcription factors and regulatory interactions in plants, Nucleic Acids Res. 45 (D1) (2017) D1040–D1045.
[58] A. Ibáñez-Salazar, S. Rosales-Mendoza, A. Rocha-Uribe, J.I. Ramírez-Alonso, I. Lara-Hernández, A. Hernández-Torres, L.M.T. Paz-Maldonado, A.S. Silva-Ramírez, B. Bañuelos-Hernández, J.L. Martínez-Salgado, Over-expression of dof-type transcription factor increases lipid production in *Chlamydomonas reinhardtii*, J. Biotechnol. 184 (2014) 27–38.
[59] C.Y. Ngan, C.-H. Wong, C. Choi, Y. Yoshinaga, K. Louie, J. Jia, C. Chen, B. Bowen, H. Cheng, L. Leonelli, Lineage-specific chromatin signatures reveal a regulator of lipid metabolism in microalgae, Nat. Plants 1 (2015) 15107.
[60] N.K. Kang, S. Jeon, S. Kwon, H.G. Koh, S.-E. Shin, B. Lee, G.-G. Choi, J.-W. Yang, B.-r. Jeong, Y.K. Chang, Effects of overexpression of a bhlh transcription factor on biomass and lipid production in Nannochloropsis salina, Biotechnol. Biofuels 8 (1) (2015) 200.
[61] S. Kwon, N.K. Kang, H.G. Koh, S.E. Shin, B. Lee, Br Jeong, Y.K. Chang, Enhancement of biomass and lipid productivity by overexpression of a bzip transcription factor in Nannochloropsis salina, Biotechnol. Bioeng. 115 (2) (2017) 331–340.
[62] C.L. Hann, C.M. Rudin, Fast, hungry and unstable: finding the achilles' heel of small-cell lung cancer, Trends Mol. Med. 13 (4) (2007) 150–157.
[63] J. Jiang, S. Srivastava, J. Zhang, Starve cancer cells of glutamine: break the spell or make a hungry monster? Cancers (Basel) 11 (6) (2019).
[64] A.K. Sharma, R. Konig, Metabolic network modeling approaches for investigating the "hungry cancer", Semin. Cancer Biol. 23 (4) (2013) 227–234.
[65] J.P. Canavate, I. Armada, J.L. Rios, I. Hachero-Cruzado, Exploring occurrence and molecular diversity of betaine lipids across taxonomy of marine microalgae, Phytochemistry 124 (2016) 68–78.
[66] J. Popko, C. Herrfurth, K. Feussner, T. Ischebeck, T. Iven, R. Haslam, M. Hamilton, O. Sayanova, J. Napier, I. Khozin-Goldberg, et al., Metabolome analysis reveals betaine lipids as major source for triglyceride formation, and the accumulation of sedoheptulose during nitrogen-starvation of *Phaeodactylum tricornutum*, PloS One 11 (10) (2016) e0164673.
[67] D.Y. Hoffmann, Y. Shachar-Hill, Do betaine lipids replace phosphatidylcholine as fatty acid editing hubs in microalgae? Front. Plant Sci. 14 (2023) 1077347.
[68] T.V. Sikorskaya, Coral lipidome: molecular species of phospholipids, glycolipids, betaine lipids, and sphingophosphonolipids, Mar. Drugs 21 (6) (2023).
[69] H. Chi, X. Wang, Y. Shao, Y. Qin, Z. Deng, L. Wang, S. Chen, Engineering and modification of microbial chassis for systems and synthetic biology, Synth Syst Biotechnol 4 (1) (2019) 25–33.
[70] A.C. Olson, C.J. Carter, The involvement of hybrid cluster protein 4, hcp4, in anaerobic metabolism in *Chlamydomonas reinhardtii*, PloS One 11 (3) (2016) e0149816.
[71] V. Subramanian, M.S.A. Wecker, A. Gerritsen, M. Boehm, W. Xiong, B. Wachter, A. Dubini, D. Gonzalez-Ballester, R.V. Antonio, M.L. Ghirardi, Ferredoxin5 deletion affects metabolism of algae during the different phases of sulfur deprivation, Plant Physiol. 181 (2) (2019) 426–441.
[72] Z. Zalutskaya, E. Minaeva, V. Filina, M. Ostroukhova, E. Ermilova, Regulation of sulfur deprivation-induced expression of the ferredoxin-encoding fdx5 gene *Chlamydomonas reinhardtii* in aerobic conditions, Plant Physiol. Biochem. 123 (2018) 18–23.
[73] C. Catalanotti, A. Dubini, V. Subramanian, W. Yang, L. Magneschi, F. Mus, M. Seibert, M.C. Posewitz, A.R. Grossman, Altered fermentative metabolism in *Chlamydomonas reinhardtii* mutants lacking pyruvate formate lyase and both pyruvate formate lyase and alcohol dehydrogenase, Plant Cell 24 (2) (2012) 692–707.
[74] A. Sawyer, Y. Bai, Y. Lu, A. Hemschemeier, T. Happe, Compartmentalisation of [fefe]-hydrogenase maturation in *Chlamydomonas reinhardtii*, Plant J. 90 (6) (2017) 1134–1143.
[75] A. de Montaigu, E. Sanz-Luque, A. Galván, E. Fernández, A soluble guanylate cyclase mediates negative signaling by ammonium on expression of nitrate reductase in Chlamydomonas, Plant Cell 22 (5) (2010) 1532–1548.
[76] J. Moseley, J. Quinn, M. Eriksson, S. Merchant, The crd1 gene encodes a putative di-iron enzyme required for photosystem i accumulation in copper deficiency and hypoxia in *Chlamydomonas reinhardtii*, EMBO J. 19 (10) (2000) 2139–2151.
[77] A. Hemschemeier, D. Casero, B. Liu, C. Benning, M. Pellegrini, T. Happe, S. S. Merchant, Copper response regulator1-dependent and -independent responses of the *Chlamydomonas reinhardtii* transcriptome to dark anoxia, Plant Cell 25 (9) (2013) 3186–3211.
[78] I.K. Blaby, A.G. Glaesener, T. Mettler, S.T. Fitz-Gibbon, S.D. Gallaher, B. Liu, N. R. Boyle, J. Kropat, M. Stitt, S. Johnson, et al., Systems-level analysis of nitrogen starvation-induced modifications of carbon metabolism in a *Chlamydomonas reinhardtii* starchless mutant, Plant Cell 25 (11) (2013) 4305–4323.
[79] G. Peers, T.B. Truong, E. Ostendorf, A. Busch, D. Elrad, A.R. Grossman, M. Hippler, K.K. Niyogi, An ancient light-harvesting protein is critical for the regulation of algal photosynthesis, Nature 462 (7272) (2009) 518–521.
[80] V. Correa-Galvis, P. Redekop, K. Guan, A. Griess, T.B. Truong, S. Wakao, K. K. Niyogi, P. Jahns, Photosystem ii subunit psbs is involved in the induction of lhcsr protein-dependent energy dissipation in *Chlamydomonas reinhardtii*, J. Biol. Chem. 291 (33) (2016) 17478–17487.
[81] J. Minagawa, Y. Takahashi, Structure, function and assembly of photosystem ii and its light-harvesting proteins, Photosynth. Res. 82 (3) (2004) 241–263.
[82] D. Elrad, K.K. Niyogi, A.R. Grossman, A major light-harvesting polypeptide of photosystem ii functions in thermal dissipation, Plant Cell 14 (8) (2002) 1801–1816.
[83] G. Bonente, M. Ballottari, T.B. Truong, T. Morosinotto, T.K. Ahn, G.R. Fleming, K. K. Niyogi, R. Bassi, Analysis of lhcsr3, a protein essential for feedback de-excitation in the green alga *Chlamydomonas reinhardtii*, PLoS Biol. 9 (1) (2011) e1000577.
[84] X. Johnson, J. Alric, Central carbon metabolism and electron transport in *Chlamydomonas reinhardtii*: metabolic constraints for carbon partitioning between oil and starch, Eukaryot. Cell 12 (6) (2013) 776–793.
[85] R.P. Gfeller, M. Gibbs, Fermentative metabolism of *Chlamydomonas reinhardtii*: I. Analysis of fermentative products from starch in dark and light, Plant Physiol. 75 (1) (1984) 212–218.
[86] R.P. Gfeller, M. Gibbs, Fermentative metabolism of *Chlamydomonas reinhardtii*: II. role of plastoquinone, Plant Physiol. 77 (2) (1985) 509–511.
[87] O. Vallon, Chlamydomonas immunophilins and parvulins: survey and critical assessment of gene models, Eukaryot. Cell 4 (2) (2005) 230–241.
[88] V. Calatrava, E.F.Y. Hom, Q. Guan, A. Llamas, E. Fernandez, A. Galvan, Genetic evidence for algal auxin production in Chlamydomonas and its role in algal-bacterial mutualism, Iscience 27 (1) (2024) 108762.
[89] S. Moret, C. Conchione, A. Srbinovska, P. Lucci, Microwave-based technique for fast and reliable extraction of organic contaminants from food, with a special focus on hydrocarbon contaminants, Foods 8 (10) (2019).
[90] D.R. Nelson, A. Chaiboonchoe, W.Q. Fu, K.M. Hazzouri, Z.Y. Huang, A. Jaiswal, S. Daakour, A. Mystikou, M. Arnoux, M. Sultana, et al., Potential for heightened sulfur-metabolic capacity in coastal subtropical microalgae, Iscience 11 (2019) 450+.
[91] G. van Zadelhoff, M. van der Stelt, Oxygenation of anandamide by lipoxygenases, in: Endocannabinoid Signaling: Methods and Protocols, 2016, pp. 217–225.
[92] T. Ito-Nagahata, C. Kurihara, M. Hasebe, A. Ishii, K. Yamashita, M. Iwabuchi, M. Sonoda, K. Fukuhara, R. Sawada, A. Matsuoka, Stilbene analogs of resveratrol improve insulin resistance through activation of ampk, Biosci. Biotechnol. Biochem. 77 (6) (2013) 1229–1235.
[93] V.G. Nielsen, M.S. Baird, L. Chen, S. Matalon, DETANONOate, a nitric oxide donor, decreases amiloride-sensitive alveolar fluid clearance in rabbits, Am. J. Respir. Crit. Care Med. 161 (4) (2000) 1154–1160.
[94] E.I. Urzica, A. Vieler, A. Hong-Hermesdorf, M.D. Page, D. Casero, S.D. Gallaher, J. Kropat, M. Pellegrini, C. Benning, S.S. Merchant, Remodeling of membrane lipids in iron-starved Chlamydomonas, J. Biol. Chem. 288 (42) (2013) 30246–30258.
[95] H. Murakami, T. Nobusawa, K. Hori, M. Shimojima, H. Ohta, Betaine lipid is crucial for adapting to low temperature and phosphate deficiency in Nannochloropsis, Plant Physiol. 177 (1) (2018) 181–193.
[96] H. Hu, L. Tan, X. Li, J. Li, C. Fan, F. Huang, Z. Zhuo, K. Hou, Y. Xu, Q. Wang, et al., Betaine reduces lipid anabolism and promotes lipid transport in mice fed a high-fat diet by influencing intestinal protein expression, Foods 11 (16) (2022).
[97] N.J. Mullen, P.K. Singh, Nucleotide metabolism: a pan-cancer metabolic dependency, Nat. Rev. Cancer 23 (5) (2023) 275–294.
[98] P.M. Gaynor, M.L. Greenberg, Regulation of cdp-diacylglycerol synthesis and utilization by inositol and choline in Schizosaccharomyces pombe, J. Bacteriol. 174 (17) (1992) 5711–5718.
[99] F.J. Fernandez-Gomez, M.F. Galindo, M. Gomez-Lazaro, V.J. Yuste, J.X. Comella, N. Aguirre, J. Jordan, Malonate induces cell death via mitochondrial potential collapse and delayed swelling through an ros-dependent pathway, Br. J. Pharmacol. 144 (4) (2005) 528–537.

[100] J. Bae, R.J. Salamon, E.B. Brandt, W.G. Paltzer, Z. Zhang, E.C. Britt, T.A. Hacker, J. Fan, A.I. Mahmoud, Malonate promotes adult cardiomyocyte proliferation and heart regeneration, Circulation 143 (20) (2021) 1973–1986.
[101] M.A.C. Reed, C. Ludwig, C.M. Bunce, F.L. Khanim, U.L. Gunther, Malonate as a ros product is associated with pyruvate carboxylase activity in acute myeloid leukaemia cells, Cancer Metab 4 (2016) 15.
[102] J. Carballo, M. Carbo, J. Pascual, M. Meijon, A. Alvarez, L. Valledor, Epigenetic dynamics in Chlamydomonas: new frontiers in unicellular algal research, Trends Plant Sci (2025). Advance Online Publication.
[103] D. Lopez, T. Hamaji, J. Kropat, P. De Hoff, M. Morselli, L. Rubbi, S. Fitz-Gibbon, S. D. Gallaher, S.S. Merchant, J. Umen, et al., Dynamic changes in the transcriptome and methylome of Chlamydomonas reinhardtii throughout its life cycle, Plant Physiol. 169 (4) (2015) 2730–2743.
[104] A. Veluchamy, X. Lin, F. Maumus, M. Rivarola, J. Bhavsar, T. Creasy, K. O'Brien, N.A. Sengamalay, L.J. Tallon, A.D. Smith, et al., Insights into the role of DNA methylation in diatoms by genome-wide profiling in Phaeodactylum tricornutum, Nat. Commun. 4 (2013) 2091.
[105] A. Zemach, I.E. McDaniel, P. Silva, D. Zilberman, Genome-wide evolutionary analysis of eukaryotic DNA methylation, Science 328 (5980) (2010) 916–919.
[106] J.H. Xue, G.D. Chen, F. Hao, H. Chen, Z. Fang, F.F. Chen, B. Pang, Q.L. Yang, X. Wei, Q.Q. Fan, et al., A vitamin-c-derived DNA modification catalysed by an algal tet homologue, Nature 569 (7757) (2019) 581–585.
[107] N. Jiang, J.S. Taylor, In vivo evidence that uv-induced c–>t mutations at dipyrimidine sites could result from the replicative bypass of cis-syn cyclobutane dimers or their deamination products, Biochemistry 32 (2) (1993) 472–481.
[108] C. von Mering, M. Huynen, D. Jaeggi, S. Schmidt, P. Bork, B. Snel, String: a database of predicted functional associations between proteins, Nucleic Acids Res. 31 (1) (2003) 258–261.
[109] D. Szklarczyk, K. Nastou, M. Koutrouli, R. Kirsch, F. Mehryary, R. Hachilif, D. Hu, M.E. Peluso, Q. Huang, T. Fang, et al., The string database in 2025: protein networks with directionality of regulation, Nucleic Acids Res. 53 (D1) (2025) D730–D737.
[110] J.M. Olson, C.A. Brewer, An evaluation of color selections to accommodate map users with color-vision impairments, Ann. Assoc. Am. Geogr. 87 (1) (1997) 103–134.